Author Version of : Geoscience Frontiers, vol.12(3); 2021; Article no: 101123

Implications of REE incorporation and host sediment influence on the origin and growth processes of ferromanganese nodules from Central Indian Ocean Basin

Simontini Sensarma[a,b*], Abhishek Saha[a*], Arghya Hazra[a,c]
[a]CSIR-National Institute of Oceanography, Dona Paula, Goa - 403004, India
[b]Indian Institute of Science, Bangalore, Karnataka – 560012, India
[c]School of Earth, Ocean and Atmospheric Sciences, Goa University, Goa - 403206, India

Abstract

This study presents new major, trace and REE data for thirty-five ferromanganese nodules recovered from areas representing three different sediment types (siliceous, red clay and their transition zone) in the Central Indian Ocean Basin (CIOB) to address their genetic aspects, classification, growth rate, nature of host sediments and influence of REE in the processes of nodule formation. The nodules from CIOB are mostly either hydrogenetic (metals coming from oxygenated bottom water), diagenetic (metals coming from suboxic sediment pore water) or a combination of both, depending on the source of supply of metal. However, a number of biogeochemical processes mediate this supply of metals which again changes from time to time, making the nodule growth process highly dynamic. This study suggests that at the initial stage of nodule growth, host sediments do not play much role in controlling the growth processes for which REEs can enter both Mn and Fe oxyhydroxide phases equally. Thus, the bottom water signature is imprinted in these early formed nodules irrespective of their host sediment substrate but with gradual growth and burial in the sediment, the main mode of metal enrichment becomes diagenetic through sediment pore water. This tends to increase the concentration of Mn, Ni and Cu over other elements which are retained in the sediment fraction. Among the REEs, Ce concentration of the nodules shows significant positive anomaly due to variation in redox potential and hence its magnitude can be used to get an idea about the metal enrichment procedure and hence the genetic type of the nodules. However, based on host sediment only, not much difference is found in the magnitude of Ce anomaly in these nodules. On the other hand, discrimination diagram, based on HFSE and REY chemistry, indicates that most of these nodules are of diagenetic in origin under oxic condition with a trend towards hydrogenetic field. Further, the genetic type of the ferromanganese nodules from the CIOB are more effectively differentiated by a combination of their major and trace element concentrations (including REY) rather than solely based on their REE or HFSE chemistry or host sediment substrate.

Keywords: Central Indian Ocean Basin, ferromanganese nodules, deep-sea sediments, rare earth elements, geochemical discrimination.

Corresponding authors: 1. Simontini Sensarma, Email: simontinisensarma@gmail.com
Phone: +91 9765108045
2. Abhishek Saha, Email: asaha.nio2015@gmail.com, asaha@nio.org
Phone: +91 832 2450334

1. Introduction:

The marine sedimentation history of the earth is marked by chemical and biochemical precipitates of varying dimensions including the manganese formations and banded iron formations (BIFs) of Precambrian times and the Ferromanganese (Fe-Mn) nodules and encrustations of modern global oceans. The former represents the primary land-based metal resources of the world, while the latter exemplifies a potential reserve for future. In fact, after Mero's (1965) calculation about the estimated *in situ* metal contents of the nodules (without giving concern about the cost it will incur on recovery and processing), a "gold rush" kind of mentality aroused back then, which gave rise to the United Nations Convention on the Law of the Sea (UNCLOS) to assure sharing of this treasure between developed and developing countries (Rona, 2008). An increasing global demand for copper, cobalt, nickel, lithium, silver, rare earth elements and other important metals concurrent with rapidly exhausting quality and quantity of terrestrial resources has put a major thrust on the exploration and exploitation of minerals in Deep Ocean. The growth of renewable energy-based technologies and multifarious applications of green technology have further driven this quest for ocean-borne mineral resources serving a pivotal role in the emerging notion of Blue Economy and sustainable industrial growth (Hein et al., 2013; Hein and Koschinsky, 2014; Hein, 2016). Mineral deposits comprising nodular concretions of predominant manganese and iron oxide/oxyhydroxide with subordinate but significant amounts of nickel, copper, cobalt, lithium, molybdenum, zirconium and rare earth elements are formed on or just below the sediment-covered surface of the deep seabed by precipitation and accretion processes around a nucleus and collectively described as ferromanganese or polymetallic nodules. Since their first recovery by *HMS Challenger* during 1873-1876 and consequent widespread researches, ferromanganese nodules have emerged as potential marine resources of metals like Mn, Fe, Cu, Ni, Co and other trace elements including Rare Earth Elements (REEs) (Friedrich et al., 1983; Glasby, 2000). Over the years, scientists all across the globe, have tried to answer the various problems posed with the exploration of manganese nodules, such as its composition, nature, accretion rate and mode of retrieval (Baturin, 1988). Although many questions could be answered, yet there are still many to be resolved. The Clarion-Clipperton fracture zone (CCZ) in the Equatorial North Pacific Ocean and the Central Indian Ocean Basin (CIOB) are the potential nodule belts of the world where their distribution and abundances are monitored by rate of sedimentation, duration of nodule accretion and availability of nucleating material. These mineral deposits are characterized by variable concentrations of Fe, Mn, Ni, Cu and Co and further discriminated as hydrothermal, hydrogenetic and diagenetic types based on the type of aqueous fluid from which the Fe-Mn oxide/oxyhydroxide precipitate (Bau et al., 2014). In contrast to Fe-Mn crusts, the nodules are

formed by precipitation from two sources such as (i) precipitation of colloidal particles directly from cold ambient seawater and accretion around a nucleus on soft sediment substrate forming hydrogenetic nodules and (ii) precipitation of metal ions either within the soft sediment or at the sediment-water interface from suboxic sediment pore waters where seawater is modified by chemical reactions within the sediment. Ferromanganese nodules of hydrothermal origin precipitate from medium to low temperature hydrothermal fluids and occur at vent sites or in diffuse-flow hydrothermal systems and have strongly fractionated Fe/Mn ratios (González et al., 2016; Josso et al., 2017). This paper presents new EPMA, major, trace and REE data for 35 ferromanganese nodules retrieved from 4500m water depth in the CIOB including areas representing three different sediment types (siliceous, red clay and their transition zone) to address (i) the salient morphological, mineralogical and geochemical attributes to evaluate their genetic aspects and classification (ii) the extent of control of host sediment for the growth processes of nodules and (iii) to evaluate whether REEs serve as better proxy than major and trace elements for discriminating genetic type of these nodules.

2. Geological and Oceanographic Settings

In the Indian Ocean scenario, the richest deposits of ferromanganese nodules are present in the Central Indian Ocean Basin (CIOB), bounded by Central Indian Ridge (CIR) in the west, South-East Indian Ridge (SEIR) in the south and Ninetyeast Ridge in the east (Mukhopadhyay et al., 2008). The abyssal depth of this area coupled with low sedimentation rate, availability of nuclei, bottom water current and highly oxic environment are conducive for nodule growth (Mukhopadhyay et al., 2008). Over the last few decades various cruises have been carried out in the CIOB and it has been found out that the maximum abundances of these nodules are spread over siliceous ooze sediment, siliceous-red clay transition and red clay sediments. The detailed description of these sediment types is reported in Sensarma et al. (2018) and the references therein. It has been reported in many earlier cases that the morphology, mineralogy and elemental concentrations of these nodules are largely affected by the type of sediment substrate on which they grow (Banakar and Jauhari, 1994; Banerjee et al., 1999; Jauhari and Pattan, 2000; Jauhari and Iyer, 2008; Pattan and Parthiban, 2011), however in ferromanganese crusts it is proved that the substrate rock does not affect crust composition (eg., Hein and Morgan, 1999; Marino et al., 2017). During 70's and 80's many attempts were taken up by both private and government organizations to mine these nodules, but none of them were successful (Glasby, 2000; Scott et al., 2006). Finally, In 2001, the International Seabed Authority (ISA) granted few nations and industrial groups an exclusive 15-year exploration contract to explore the areas of the most prospective manganese nodules (combined Cu, Ni, Co content >2.5% by weight, abundance >10 kg/m^2) in the CCZ and CIOB (Rona, 2008). This

resulted in 1,500,000km^2 area of R&D activities in the CIOB which culminated into 750,000km^2 area of First Generation Mine Site (FGM) (Jauhari and Pattan, 2000).

3. Materials and methods

3.1. Study area and sampling

The nodule samples were collected by free fall grabs at 35 locations in the CIOB, broadly between 10^0 and 16^0S latitude and 74^0 and 84^0E longitude, covering mostly siliceous sediments (21 samples), red clay (7 samples) and their transition zone (7 samples). The water depth varied from 4800m to 5700m below mean sea level (MSL) with an average water depth of 5200m. All these nodule samples were collected during various cruises of MV Skandi Surveyor, AA Sidorenko and AB Petrov, as a part of the "project surveys for polymetallic nodules" in the CIOB. The sample locations are presented in Fig 1 and Table 1. These are all surface samples i.e., residing within top 0-5cm of the sediment column. After collection, the samples were washed thoroughly with deionized water, dried and stored in plastic zip pouches at room temperature.

3.2. Mineral identification

The nodule samples were oven dried overnight at 60^0C, hand ground into very fine powders and kept in desiccators prior to the analysis. Then few grams of each sample were adhered onto glass slides by pressing the powdered samples with another glass slide. These slides were then analyzed in an X-ray diffractometer (Rigaku – Ultima IV) using nickel filtered Cu Kα radiation operated at 40kV power and 20mA current, from 5-70^0 2θ min^{-1}. The database used for mineral identification is webmineral.com. It contains descriptions of 4,714 individual mineral species with links and a comprehensive image library. Each mineral has a page linked to tables devoted to crystallography, crystal structures, X-Ray powder diffraction, chemical composition, physical and optical properties. There are also extensive links to other external sources of mineral data and information which were used for cross-referring.

3.3. Major and trace element analysis

Iron and manganese concentrations of the nodule samples were analyzed in a Perkin Elmer AAnalyst 200 Flame Atomic Absorbtion Spectrometer (FAAS). Although the same solutions were used for both major and trace element analyses, the solutions were diluted many times for Fe (2-4 times) and Mn (6-13 times) due to their very high concentrations in nodule samples. The trace elements including Rare Earth Elements (REEs) were analyzed in an X-Series II (Thermo Fisher) quadrupole Inductively Coupled Plasma-Mass Spectrometer (ICP-MS). Twenty milligram of powdered samples were taken for each nodule samples and were completely digested with acid mixture HF:HNO_3:$HClO_4$ in the ratio 7:3:1 on a hot plate. In addition, 4ml of

1:1 HCl solutions were added to each sample and heated on a hot plate till totally digested. After that, the samples were dissolved in 4ml of 1:1 HNO_3 solution and transferred into 100ml volumetric flask by filtering. Internal standard ^{103}Rh solution (1ng/ml) was added to each of them and volume was made up to 100ml with Milli-Q water (modified after Banerjee et al., 2018). Atlantic and Pacific nodule standards NOD A-1 and NOD P-1 were used as certified reference materials for both major and trace metal analyses. The element concentrations are given in Table 1 and 2.

3.4. Elemental analysis of nodule microlayers by EPMA

The chemical composition of the nodule growth rims was determined with CAMECA SX Five Electron Probe Micro Analyzer at CSIR-National Institute of Oceanography (NIO), Goa, India. The analyses were performed on carbon coated polished thin sections with 15kV accelerating voltage and 8-10nA beam current. The particles were measured with a 10µm beam. Natural mineral standards (diopside for Si, plagioclase feldspar for Al, pyrrhotite for Fe, pentlandite for Ni, chalcopyrite for Cu and sphalerite for Zn) along with synthetic metal oxide standards for Mn and Co were used for calibration. The precision of the analysis is better than 1% for major element oxides from the repeated analysis of standards. The average chemical data of the microlayers of representative nodules are given in Table 3 and that of each microlayers of few nodules are given in Table S1 of supplementary data.

4. Results

4.1. Nodule morphology

The shape of the studied nodules from CIOB varies from sub-rounded, ellipsoidal, irregular, globular to elongate (Fig 2). Some of the nodules are slightly triangular in shape (sample numbers 190A, 428A, 467, 211A and 239A) owing to the shape of the nucleus. It has been observed in many cases that the nodules with shark or fish tooth as nuclei tend to grow in a triangular manner. Their average long axis dimension is between 1 and 5cm, with few of them (11 out of 35) having greater than 5cm. The nodules from siliceous and transition zones are mostly rough to gritty textured with comparatively thicker oxide layers (1-3mm). Only four nodules from these two sediment types have completely smooth surface texture (sample numbers 139, 301, 319 and 267C). On the other hand, most of the nodules from red clay sediment have smooth texture except two (235E and 254D) and much thinner oxide layers (0.5-2mm). Out of these 35 nodules, most are polynucleated with the exception of three from siliceous domain (467, 301 and 139), one from transition zone (267C) and two from red clay domain (211A and 239A). The density of the nodules increases from 1.9 to 2.2g/cm^3 as their porosity decrease from siliceous zone towards red clay zone (from 62.98 to 58.92). In general, there is hardly any difference of morphology between

the nodules from the siliceous and transition zone, except for some nodules from transition zone has a smoother upper surface than the lower one. However, the nodules from red clay sediment domain are morphologically distinct from the nodules of siliceous and transition zone (Fig 2).

4.2. Nodule Mineralogy

The predominant Fe-Mn oxyhydroxide bearing mineral phases identified in these nodules include the 10Å manganite phase (todorokite or buserite) and δMnO_2 phase (vernadite). XRD studies for most of the samples reveal two prominent peaks of 10Å manganite phase, one between 9.7 and 10Å and the other in the range of 4.7 to 5.02Å (Fig 3). Although XRD data alone could not confirm whether this phase was todorokite or buserite (Burns et al., 1985), however, due to the abundance of todorokite in the CIOB nodules (Banerjee and Mukhopadhyay, 1990; 1991; Banerjee et al, 1999; Jauhari and Pattan, 2000), this phase is henceforth referred to as todorokite in the text all through. Vernadite, on the other hand, showed a peak in the range of 2.37 to 2.47Å (Fig 3). It has been reported in many cases that iron might be present in the form of FeOOH as fine-scale epitaxial intergrowth with vernadite (Burns and Burns, 1979; Ostwald, 1984; Manceau et al., 1992), which might be possible in this case also. Another mineral found to be ubiquitous in all the nodule samples, with a sharp peak at 3.32-3.34Å interval, was quartz (Fig 3). As nodules grow in layers, some layers accumulate more ferro-manganese oxide minerals whereas, some contain more detrital minerals. This feature is attributed to the variation in redox potential of the depositional environment through time. Hence, the layers comparatively deprived of ferro-manganese minerals tend to accrete quartz as the major detrital mineral. Apart from quartz, the other accessory minerals found to be associated with the nodules of this area include anorthite (3.2Å), albite (3.17Å) (Fig 3a), and nontronite (4.46Å) (Fig 3b).

4.3. Bulk nodule Chemistry

The concentrations of Fe, Mn, Co, Ni, Cu, Zr and REEs for the nodules from the study area are given in Table 1 and 2. Both the highest and lowest concentrations of Fe, Mn, Co, Cu, Zr and ∑REY are found in the nodules from siliceous sediment (Table 1 and 2). Highest concentration of Ni is also found from this zone (sample number 133E; Ni ~ 1.62%), while its lowest concentration is found from red clay zone (sample number 211A; Ni ~ 0.58%). Mn/Fe ratio varied from as high as 14 to as low as 1.56 with an average value of 5.16. Compared to the other two sediment types, the overall metal concentrations of the nodules from the transition zone are low. However, the average Mn, Ni and Cu concentrations are high in the nodules from this zone and Zr concentration is intermediate (Table 4). Although no element was found to show highest concentrations in the nodules from red clay zone, average concentrations of Fe and Co were found to be higher in the red clay zone nodules than the other sediment types (Table 4). The

nodule (sample number 162) having the highest Mn concentration (45.85%) also shows the lowest Co (0.06%), some REEs (La-Sm and Tb) and ∑REY concentrations (663.6ppm) with a corresponding highest Mn/Fe value of 14. On the other hand, the sample 317 having the highest concentrations of Fe (10.83%), Co and Zr (2400 and 1491.0 ppm respectively) also displays highest concentrations of Nd, Gd and Y with a corresponding lowest Cu concentration (0.37%) and Mn/Fe ratio of 1.56. Lowest concentration of Fe (2.84%) corresponded with the highest concentration of Cu (1.51%) in the sample 318F. Again, highest concentrations of some REEs (La, Ce, Sm, Eu, Tb, Dy, Ho-Lu) and ∑REY (2806.0ppm) is found in sample number 309, which has neither the highest concentration of Fe nor Mn but corresponds to the lowest concentration of Cu (0.37%).

4.4. EPMA analysis

4.4.1. Texure

Back scattered electron (BSE) images of the selected nodule samples along their cross-section reveals alternate Fe and Mn-rich layers with various types of nucleus in the core. For instance, plagioclase grains are a very common nucleating material (Fig 4b) along with fresh/altered basalts (Fig 4c and 4e). Another common nucleating material is shark tooth and/or fish tooth, which is observed in this case also (Fig 4d and 4f). The Mn-rich layers are pale grey to almost white in colour as they appear brighter than the Fe-rich layers which are darker in shade (Fig 4). Sometimes the microlayers are continuous for considerable thicknesses (Fig 4a). They vary from dendritic (outer rims in Fig 4a), laminated (Fig 4c), and globular (Fig 4e) types. Multiple microstructural types are present in all nodules irrespective of host sediment types and these occasionally interfere with or merge into one another. Surface layers of rough-textured nodules exhibit mainly dendritic microstructures (outer rims in Fig 4a) whereas, smooth nodules exhibit laminated microstructure mostly (Fig 4c), although dendritic growth patterns can also be observed. These microstructures are also formed by colloform growth (Fig 4b and 4e). Microlayers are generally discrete but commonly lack lateral continuity (Fig 4d). Post-depositional changes are also recorded in many nodules as radial cracks (macroscopic and microscopic) which are formed by late stage dehydration (Cronan, 1980; Heath, 1981; Friedrich et al., 1983). These cracks are either restricted to specific depth zones intruding into younger oxide laminae only (Fig 4c), or may cross-cut the entire nodule postdating the nodule growth (Fig 4a).

4.4.2. Mineral chemistry

Electron microprobe analyses show that nodules from all the three sediment types host mixed type nodules with alternate Fe and Mn-rich layers (sample no. 262, 291 and 201F in Table

S1). They have comparatively higher Cu and Ni concentrations than Co concentration and Mn/Fe ratio as high as ~450 in certain layers. On the other hand, the hydrogenetic type nodule (sample no. 139 in Table S1) has much higher concentrations of both Fe and Co than the other three nodules, although its host sediment is siliceous ooze. Certain layers (datasets/points in Table S1) have very low metal concentrations due to higher amount of Al and Si present in them (Table 3) which indicates the presence of finely intermixed detrital phases. The presence of plagioclase grain (Fig 4b; points 1-6 of sample no. 291 in Table S1) or fresh/altered basalts (Fig 4c and 4e; sample no. 139 in Table S1) in the core of some nodules further increases Al and Si concentrations in them. However, shark tooth and/or fish tooth found in some nodule cores (Fig 4d and 4f; sample no. 201F) exhibit low concentrations of both detrital and metal phases (points 1-9 of sample no. 201F in Table S1). Copper and nickel contents when plotted against Mn/Fe ratio of these microlayers, exhibit positive regression relation (Fig 5a and 5b) whereas, cobalt content shows negative regression relation with Mn/Fe ratio (Fig 5c).

4.5. Calculation of growth rate

Growth rate of the nodules was calculated from the Mn and Fe concentrations of the nodules, following Lyle's equation below (1982):

$R = 16.0 \times (E_{Mn}/[E_{Fe}]^2) + 0.448$…….[Eq. 1]

Where, R = growth rate of the nodules in mm/10^6years, E_{Mn} and E_{Fe} = elemental concentrations of Mn and Fe in the nodule samples. Following this equation, the growth rate of the nodules of the present study varied from as low as 2.75 (sample number 317) to as high as 68.89mm/10^6 yrs. (sample number 162). However, it was stated in Lyle (1982) that in absence of measured growth rates, the above equation can be used reliably to estimate the nodule growth rates from their compositions only up to rates of about 50 mm/10^6 yrs. Fast growing nodules do not follow the relationship of Mn accumulating at a rate proportional to the square of the Fe accumulation rate, based on which the above equation was made. Hence, the nodule sample exhibiting 68.89mm/10^6yrs. growth rate could be an over estimation and henceforth been ignored from the rest of the discussion. So, the highest growth rate found in this study was 40.18mm/10^6 yrs. in the sample 318F. It can be seen from Table 4 that in individual sediment type, transition zone had the highest average growth rate of 22.54mm/10^6yrs, followed by siliceous sediment (18.03mm/10^6yrs) and least in the red clay domain (11.91mm/10^6yrs).

5. Discussion

5.1. Nodule Classification

Various classification schemes have been espoused to constrain the genetic types for ferromanganese nodules owing to their morphological, mineralogical and geochemical diversity (Halbach et al., 1981; Aplin and Cronan, 1985; Halbach et al., 1988; Bonatti et al., 1972; Hein et al., 1997). The most common among them is the Fe-Mn-(Cu+Ni+Co)x10 ternary diagram (after Halbach et al., 1981) which classifies the nodules as hydrogenetic, diagenetic and hydrothermal based on their modes of origin. Recent studies by different researchers have used trace elements and REE concentrations for classification of nodules (Bau et al., 2014; Schmidt et al., 2014; Hein et al., 2016; Pelleter et al., 2017; Josso et al., 2017). However, all these classification schemes are environment specific and cannot be generalized for all types of Fe-Mn formations. This is in particular applicable for CIOB nodules, as the influence of hydrothermal source is negligible in this case (Glasby, 1973; Jauhari and Iyer, 2008). The nodules found in this region are mostly formed by hydrogenetic or diagenetic processes or a combination of both. Only near the ridge crests where some hydrothermal activities are observed, nodules and crusts grow via hydrothermal plume fall out. Hence, most of the elements are either derived from the oxic bottom water or suboxic porewater. Again, these two end-members are not mutually exclusive. With continuous sedimentation, bottom water activity, burrowing of benthic fauna and other physico-chemical factors, considerable overlap occurs between these two end members. Recent work on mineral transformation within nodules from Clarion and Clipperton Zone of the equatorial Pacific Ocean have shown that the nodules of partly or even fully buried nodules also exhibit alternate hydrogenetic and diagenetic layered growth structures which indicates that the marine environment, under which these nodules are forming, varied throughout the time (Wegorzewski et al., 2020). This has been mentioned by Bau et al. (2014) also that, pure end member nodules are very rare to find and their diverse mineralogical composition poses a challenge for any one particular geochemical discrimination scheme to effectively distinguish between different types of crusts and nodules.

On the basis of Fe-Mn-[(Ni+Cu+Co)x10] ternary diagram as per Halbach et al. (1981), 16 out of these 35 studied nodules from CIOB are of early diagenetic type or Type A, 15 are of mixed type or Type AB and remaining 4 are of hydrogenetic type or Type B (Table 1 and Fig 6). Whereas, based on the discrimination diagram proposed by Josso et al. (2017), most of the nodules fall on the oxic diagenetic field with a continuum towards hydrogenetic field (Fig 7). Only, two nodules from siliceous zone fall completely in the hydrogenetic field in this diagram (Fig 7). On the other hand, following the geochemical discrimination diagram of Bau et al. (2014), most of

the nodules from present study fall in the hydrogenetic to mixed fields (Fig 8). The aqueous speciation of trace elements dictates their association with Mn or Fe oxide phases, as Mn oxides are generally negatively charged under seawater conditions, whereas Fe oxyhydroxides are neutral or slightly positively charged (Koschinsky and Halbach, 1995; Sensarma et al., 2016). The porous nature of the nodules allows the penetration of surrounding waters into them, thereby causing both chemical and mineralogical changes if the water chemistry changes with time (Blöthe et al., 2015). Under oxic conditions, hydrogenetic layers are formed due to metal precipitation from oxic seawater mainly. Those layers consist of vernadite, which has epitaxial intergrowth of amorphous Fe-oxyhydroxides (δ-FeO OH) and contain low amount of Cu^{2+} (0.34 ± 0.16 wt.%; Wegorzewski and Kuhn, 2014), which is found in this study also (sample no. 139 in Table S1). b). The incorporation mechanism of these metals into todorokite is less documented (Manceau et al., 2014; Atkins et al., 2016; Wu et al., 2019). Nevertheless, it is known that Mn^{4+} occupies the central and edge sites of the triple chains of todorokite tunnels while Mn^{3+}, Ni^{2+} and Cu^{2+} exclusively occupy the edge sites (Post and Bish, 1988; Bodeï et al., 2007, Manceau et al., 2014). Furthermore, metals such as Ni^{2+} can also form an outer-sphere complex in the todorokite tunnels (Pakarinen et al., 2010). That is why concentrations of Ni and Cu in diagenetic and mixed type of nodules is more than Co. However, till date, there are no data about the location of Co or REEs into the todorokite structure of naturally occurring Fe-Mn nodules. Hence, considering all the above points, using REE chemistry to discriminate genetic classifications of deep-sea nodules can be erroneous.

5.2. Influence of host sediment on nodule growth process

It has been envisaged that in the CIOB the area between 10-16^{0}S latitude (Fig 1) is a high relief zone with a number of seamounts and abyssal hills (Jauhari and Iyer, 2008; Table 5). The low sedimentation rate and high surface productivity of this zone make this area ideal for nodule formation (Jauhari and Iyer, 2008; Mukhopadhyay et al., 2008). Sediment pore fluids are the predominant source of Ni, Cu, and Mn contents of the investigated CIOB ferromanganese nodules while Fe, Co, Zr, REEs and Y (together ΣREY) are derived predominantly from the seawater (Jauhari and Iyer, 2008; Mukhopadhyay et al., 2008; Josso et al., 2017). The metal enrichment for nodules growing over siliceous sediments is ascribed to the porous nature of the host sediment and associated pore waters. These features account for the diagenetic nature of the nodules which contain todorokite as the main Fe-Mn oxyhydroxide bearing mineral. Price and Calvert (1970) suggested that, although divalent cations can easily enter into todorokite structure, presence of organic matter can prevent nodules from being enriched in minor elements (Price, 1967). This is applicable particularly for Cu, Ni and Co. The formation of stable organo-metallic complexes within the sediment would inhibit metal uptake into Fe-Mn oxides. The order of stability of water-

soluble, organo-metallic complexes is as follows: Mo, V<Zn<Cu<Co<Ni (Kee and Bloomfield, 1961). In fact, according to various authors (Boström et al., 1974; Manceau et al., 2014), Cu may also be associated with organic matter, biogenic silica, phosphates, carbonates or aluminosilicates. In some recent studies, It has been shown through FT-EXAFS analysis as well as leaching experiments of surface and buried nodules that, Cu is strongly associated with Mn-oxides and to a lesser degree with Fe-oxyhydroxides and not with other phases in the Mn nodules from Pacific ocean (e.g., Wegorzewski et al., 2020; Mohwinkel et al., 2014; Wegorzewski and Kuhn, 2014; Heller et al., 2018). Similar phenomenon has also been noticed in the nodule associated sediments of CIOB (Sensarma et al., 2016, 2018). The presence of Cu bound to organic matter is negligible in deep-sea oxic environment as the total organic carbon content in these nodules is ~0.05% (Wegorzewski et al., 2020) and that of associated sediments is ~0.56% (Sensarma et al., 2016). Although it can be seen from the EPMA data that very high Mn concentration in certain microlayers correspond to much less Cu, Ni and Co concentrations (points 8-17 of sample 291 in Table S1), that is mainly due to transformation of Mn phyllomanganates (eg: vernadite) to tectomanganates (eg: todorokite) which inherently contains less trace elements (Wegorzewski et al., 2020). That is why, Mn concentration of studied nodules from siliceous sediment is not showing significant positive correlation with any trace elements or REEs (Table 6a). In fact, Mn has no significant correlation with any elements in nodules from all sediment types (Table 6). This is in contrast with previous reports where significant positive correlation was observed between Mn, Cu and Ni concentrations of CIOB nodules (Banerjee and Mukhopadhyay, 1990; Pattan and Parthiban, 2011). Moreover, two nodules from this sediment type are found to be hydrogenetic in nature (139 and 317), both having considerably high concentration of Fe (highest in 317) and relatively low Mn/Fe ratios. Microprobe analysis of nodule sample 139 reveals very high Fe concentrations (points 6-11 and 14-21 in Table S1) corresponding to significantly higher Co concentration than the other nodules (Table S1). Hydrogenetic nodules not only contain vernadite as dominant ferromanganese mineral, but also todorokite to some extent as evident from this study. This also complies with hydrogenetic nodules and crusts from the Atlantic Ocean, containing todorokite (Marino et al., 2018) or nodules with todorokite and romanechite in the Galicia Bank (González et al., 2016). In contrast to this, vernadite is more prominently present in nodules of mixed origin (267C and 201F; Table 1).

On the other hand, water depth in the transition region is deepest in the study area, with an average of 5238.5m below mean sea level. Moreover, this area falls within the moderately low productivity zone of abyssal plain (closer to red clay domain, hence less bio-productive, evident from Table 5 and Fig 1) where the metal enrichment mechanisms by both early diagenetic and hydrogenetic procedures are active (Bonatti et al., 1972; Burns and Burns, 1979). Hence, the

nodules, found in this area showed a distinct gradation consisting of an upper smoother surface and a lower rough to gritty surface due to hydrogenetic metal enrichment in the sediment-water interface and early diagenetic in the partly buried portion. They are comparatively bigger in size than the nodules resting on siliceous and red clay sediments with an average diameter of 5cm. Their dominant shape and size are very similar to the Pacific Ocean nodules which are also bigger in size with diameters of up to 14cm (Halbach et al., 1981). The average growth rate of these nodules is 22.41mm/10^6yrs which is the highest in the study area. However, the occurrence of both mixed and diagenetic type nodules here can be translated in terms of the predominance of either hydrogenetic or diagenetic mechanism influencing the growth of a particular nodule. The average concentrations of Ni and Cu were found out to be higher in these nodules than from the other two sediment types (Table 4), as enrichment of transitional elements in Fe-Mn deposits goes in the order: oxic-diagenetic > hydrogenous >suboxic-diagenetic > hydrothermal (Dymond et al., 1984; Takematsu et al., 1989). This is also evident from EPMA analysis of nodule sample 262 (points 1-7 in Table S1) where concentrations of Ni and Cu are comparatively much higher than Co.

Zirconium concentrations of nodules from both transition and red clay zone do not show any significant correlation with either Fe, Co or ΣREY concentrations unlike the nodules from siliceous host. Although Zr is dominantly incorporated through hydroxides (Bruland, 1983; Bau et al., 1996; Josso et al., 2017), it did not show any such association with other hydrogenetically complexed element like Fe, Co or ΣREY in the nodules from transition zone and red clay. In fact, average concentration of Zr decreased in nodules from siliceous host, to transition zone and least from red clay host (Table 4). This is because a significant amount of Zr is contributed from land derived detritus in the form of aeolian source such as loess (Schnetger, 1992) and Saharan desert (Wehausen & Brumsack, 1999) in this part of the ocean. Similar observation was also made in Sensarma et al. (2018) where Zr is found more towards the northern part of the study area, for which nodules from those areas contain higher concentration of this element inherently than the nodules from the lower part of the study area and so far there are no reliable data available on the metal incorporation mechanism of Zr in deep-sea nodules.

The average concentrations of Cu and Ni are lowest in nodules from red clay sediment but have highest Fe and Co concentrations. The main source of metal here is from oxygenated bottom water and additional supply from the sediments is negligible due to impervious nature of clay. Hence, Fe and Co are preferentially incorporated in these nodules over Mn, Cu and Ni for which growth rate also reduces considerably for these nodules. However, except two, most of the nodules from red clay zone are of mixed type and one of them is even diagenetic in nature (237B). Here, it has to be kept in mind that the entire division of nodule types into diagenetic or

hydrogenetic is entirely based on their dominant characteristics (chemistry, mineralogy etc.) and do not necessarily represents individual layers. Based on the maximum Fe-Mn oxide layer thickness and the average estimated growth rates in Table 4, the growth interval of the oxide layers can be calculated as ~0.15 Myr on average. The surface ocean productivity in the studied area could have fluctuated during this interval. Therefore, the genetic features of the nodules might be influenced not only by spatial factors but also by temporal factors. The widely varying Mn/Fe ratios (1.6-14) for the studied CIOB nodules corroborate a hydrogenetic-diagenetic spectrum with distinct signatures of interaction between these two processes. This is even more evident from Fig 7 where a clear trend is seen from oxic diagenetic to hydrogenetic field of the nodules from the present study. However, in this discrimination diagram only two nodules from siliceous zone fall completely in the hydrogenetic field. The nodules (211A and 239A) from red clay area, which are in the hydrogenetic field in Fig 6 are not falling in hydrogenetic field in Fig 7, although their morphology, mineralogy, major and trace element chemistry (except Zr) all indicate towards hydrogenetic origin. The reason for this contradiction probably lies in the inherent low concentration of Zr in the nodules from red clay zone as both Ce and Y concentrations are high in them. Thus, nature of Zr cannot be considered hydrogenetic entirely and caution should be taken while using discrimination diagram based on High Field Strength Element (HFSE) for nodule classification.

5.3. REE incorporation in the nodules: the hydrogenetic-diagenetic conundrum

Post Archean Australian Shale (PAAS) normalized REE concentrations (including Y) of all the nodules have similar distribution pattern with a prominent positive Ce anomaly and negative Y anomaly, which is typical for deep-sea ferromanganese nodules (Fig 9). When classified according to sediment type, the nodules from red clay sediment exhibited slightly higher average REE concentrations than the siliceous and transition zone nodules (Fig 9a). However, when classified according to genetic type (as per Halbach et al., 1981) hydrogenetic nodules showed much higher average REE concentrations than the diagenetic and mixed type nodules (Fig 9b). The REE and HFSE concentrations in ferromanganese nodules are primarily attributed to the hydrogenetic component while, enrichment in metallic elements like Mn, Cu, Ni and Zn is derived through diagenetic precipitations (Josso et al., 2017). To check the applicability of the discrimination scheme proposed by Bau et al. (2014) in the present case, data of different Fe-Mn deposits from different oceans are also plotted here (Fig 8). All the normalization here are based on Post Archean Australian Shale (PAAS) values and calculation of Ce/Ce* is done as per Bau et al. (2014). Since REEs do not form phases of their own in nodules, proper identification of possible mineral phases governing REE incorporation is needed before applying the above discrimination scheme. In surficial waters, Ce can enter the manganese oxyhydroxide structure as

a result of the oxidation of Mn^{2+} and Ce^{3+} on the surface of suspended particulates (Moffett, 1990; Sholkovitz et al., 1994). Thus, when nodules start growing, they inherit the compositional signature of ambient bottom water. However, during the subsequent growth stages, the role of sediment pore fluid, associated with host sediments, becomes increasingly dominant (Dubinin and Sval'nov, 2000a). In high bio-productive zones like Guatemala basin, Peru basin of Pacific Ocean, Mn accumulation in surficial sediment layer is related to its remobilization from sediments due to the reduction by organic matter and the subsequent oxidation of Mn by oxygenated bottom water (Dubinin and Sval'nov, 2000b). But the absorbed REE assemblage is retained during the process. The high intensity of reduction, transportation to the sediment surface, and oxidation of Mn by the dissolved oxygen results in the formation of Mn-rich nodules, in which the Fe concentration rarely exceeds 3% (Dymond et al., 1984; Murphy and Dymond, 1984; Dubinin, 1996). The growth of nodules is accompanied by increase of Mn/Fe ratio thereby suggesting an intense supply of the reduced Mn from sediments in conjunction with decreased uptake of Co but increased uptake of Cu and Ni into Mn oxyhydroxides. These compositional transformations cannot be equated with a simple mixing of hydrogenetic and diagenetic materials; rather they are attributed to the prevalence of hydrogenetic material at the initial nodule-forming stage and the primary supply of material from the underlying sediment. In addition to the supply of metals, difference in Mn-oxide minerals can affect the feature of concentration of metals. For example, δ-MnO_2 oxidize dissolved Ce (III) and Co (II) to Ce (IV) and Co (III), respectively, and incorporate them into the crystal structure (e.g. Ohta & Kawabe, 2001; Takahashi et al., 2007). That is why, although hydrogenetic Fe-Mn crusts of CIR (Banerjee et al., 2018), Atlantic (Baturin and Dubinchuk, 2011; Muinos et al., 2013; Marino et al., 2017 and 2018), hydrogenetic nodules of south-central Pacific (Hein et al., 2015), hydrothermal crusts from south-west Pacific (Josso et al., 2017) and hydrogenetic-hydrothermal crusts from Ninetyeast Ridge (Hein et al., 2016) are all falling in their designated fields (Fig 8a and 8b), the CIOB nodules from this study, Pattan and Parthiban (2011), Pattan and Banakar (1993) and central and north-eastern Pacific (Ohta et al., 1999) are largely corresponding to the hydrogenetic to mixed field (Fig 8a and 8b), though this classification may not entirely reflect their actual genetic type. The CIR crusts from Kuhn et al. (1998) are very different in characteristics. They are termed as mixed hydrothermal-hydrogenetic in nature, although they fall in the diagenetic field mostly (Fig 8b). One of the samples from Marino et al. (2017) fall alongside the same cluster as that of Kuhn et al. (1998) in Fig 8a and fall in the hydrothermal field in Fig 8b along with one of the samples from Hein et al. (2016). However, Bau et al. (2014) has explained this unusual nature as due to exceptional fast growth of these crusts that prevented the preferential accumulation of Ce.

The enrichment of REEs in Fe-Mn deposits goes in this order: hydrogenous >oxic-diagenetic >suboxic-diagenetic > hydrothermal (Dymond et al., 1984; Takematsu et al., 1989). The less enrichment of REE in oxic-diagenetic nodules than the hydrogenetic type, in contrast to transition elements, is equated with lower concentration of REEs in sediment pore waters than seawater or greater retention of REEs in sedimentary phases than transition elements during diagenetic remobilization (Takematsu et al., 1989). That is why, highest concentrations of Cu and Ni are found in the nodules from transition zone and Co from red clay zone (Table S1). On the other hand, PAAS normalized REE pattern showed significantly higher values in hydrogenetic nodules than other genetic types (Fig 9b) which is not observed when differentiated on the basis of host sediment only (Fig 9a). REEs not only enter Fe-rich phases but also Mn-rich phases. The significant positive correlation of REEs with Fe is ascribed to their similar supply mechanism and not due to the incorporation of REEs in to Fe-oxyhydroxide phase (Takematsu et al., 1989). That is why highest concentrations of some REEs and ∑REY are found in nodule sample 309, from siliceous sediment which has very low Fe concentration but quite high Mn (Table 1 and 2). Thus, it can be inferred that with the subsequent growth of nodules, the characteristics of their genetic type also changes according to the source of supply of metals. At the initial stage of nodule formation, the metal incorporation is mainly through oxygenated bottom water (Fig 10a-c), irrespective of the host sediment character. That is why hydrogenetic nodules are also found in siliceous sediment. But in siliceous zone, due to high sedimentation rate, the nodules get buried under sediment cover with time which cuts off the hydrogenetic source of metal supply largely. The main source is then switched to sediment pore water, due to early diagenetic remobilization of redox sensitive metals, among which Mn has the highest mobility than any other elements (Fig 10d). On the other hand, in the transition zone, sedimentation rate is moderate for which the nodules from this zone receive metals via both hydrogenetic and diagenetic sources (Fig 10e) while, in red clay area the main source of metal input remains to be authigenic due to low porosity and permeability of the sediment (Fig 10f). The effect of very low sedimentation rate in red clay area is also an important factor here which results in long time exposure of the nodule on the seafloor, enabling them to incorporate the hydrogenetic metals such as Ce and Co.

Relative abundances and anomalies of redox-sensitive REE like Ce and redox-insensitive elements like La, Gd and Y on REY patterns provide significant insights into REY fractionation or partitioning and incorporation during precipitation of Fe (III) oxides/hydroxides and Mn (IV) oxide from water column in ocean. In this study, the REE + Y signatures manifested in terms of positive Ce anomalies, Y_N/Ho_N <1 and negative Y anomalies collectively substantiate the hydrogenetic nature of the studied CIOB nodules. The negative Y anomalies and $Y_N/Ho_N < 1$ reflect Y fractionation in the water column and lower stability of Y in hydroxide complexes. The

variation in the magnitudes of Ce anomalies for the studied CIOB nodules can be correlated with genetic aspects of their growth rate. The hydrogenetic nodules in this study exhibit greater magnitude of positive Ce anomalies as compared to the nodules of diagenetic and mixed character thereby indicating a very slow growth rate. Thus, major, trace and REE chemistry for the CIOB nodules provide a dimension to the hydrogenetic-diagenetic conundrum. The Mn-Fe compositions correspond to their diagenetic to hydrogenetic spectrum, whereas REE + Y chemistry substantiates the hydrogenetic trait with mild mixed character.

6. Conclusions

The genetic type of the ferromanganese nodules from Central Indian Ocean Basin are more effectively differentiated by their major and trace element concentrations than their REE and HFSE concentrations or host sediment substrate. At the initial stage of growth of these nodules, the host sediments do not control the metal enrichment procedure much for which REEs can enter both Mn and Fe oxyhydroxide phase from ambient bottom water. That is why hydrogenetic type nodules are also found in siliceous sediment and quite high concentrations of some REEs are found in few nodules from this area having significantly higher Mn concentration than Fe. But with subsequent growth of the nodules, increased supply of reduced metals via sediment pore water becomes more important due to early diagenetic effect. This tends to increase the concentrations of Mn, Cu and Ni in the nodules over other metals. Thus, the significant positive correlation of REEs with Fe is not just due to their incorporation in the same phase but due to their similar supply mechanism in the nodules. Among the REEs, only Ce concentration of the nodules shows significant positive anomaly due to variation in redox potential of the marine environment and hence its magnitude can be used to get an idea about the metal enrichment procedure and hence the genetic type of the nodules. However, based on host sediment only, not much differences are found between the magnitude of Ce anomaly in these nodules. This is because a single nodule can show hydrogenetic signature at the initial stage of growth and then change into mixed or diagenetic type depending on the source of supply metals. On the other hand, due to considerable supply of Zr (HFSE) from land detritus, nodules from siliceous ooze zone, which is closer to landmass, inherently contains more of this element than those further away from land, although concentrations of Fe, Co and REEs are more in the nodules from red clay host. Thus, caution should be taken while applying different geochemical discrimination schemes on ferromanganese nodules as their growth process is rather complex than envisaged in these schemes.

Acknowledgements

The authors are thankful to the Director, CSIR-NIO, Goa for permitting to carry out this work. Dr. Ranadip Banerjee is thanked for providing the required samples and Dr. Subir Mukhopadhyay is thanked for his invaluable suggestions. Dr. Durbar Ray, Dr. Alagarsamy, Ms. Seyieleno C Seleyi and Ms. Charmaine L Fernandes are thanked for helping in FAAS analysis and Mr. Pushkaraj Shirodkar is thanked for assisting in taking images of the nodule hand specimens. SS gratefully acknowledges the support of CSIR Senior Research Fellowship, India. The authors sincerely acknowledge the facilities received from Central Analytical Facility, CSIR-NIO. Mr. V.D. Khedekar is duly acknowledged for providing the EPMA data. The authors are thankful to the handling Associate Editor Dr. Inna Safonova and three anonymous reviewers for their insightful suggestions which have greatly improved the quality of the manuscript. This work is a part of the "Polymetallic Nodule: Survey and Exploration" project (GAP 2175) supported by Ministry of Earth Sciences, Govt. of India. This is NIO's contribution No. XXXX.

Reference

Aplin, A.C., Cronan, D.S., 1985. Ferromanganese oxide deposits from the central Pacific Ocean, II. Nodules and associated sediments. Geochimica et Cosmochimica Acta 49, 437-451.

Atkins, A.L., Shaw, S., Peacock, C.L., 2016. Release of Ni from birnessite during transformation of birnessite to todorokite: Implications for Ni cycling in marine sediments. Geochimica et Cosmochimica Acta 189, 158–183.

Banakar, V.K., Jauhari, P., 1994. Geochemical trends in the sediments and manganese nodules from a part of the Central Indian Basin. Journal of Geological Society of India 43, 591-598.

Banerjee, R., Mukhopadhyay, R., 1990. Characteristics of manganese nodules from sub-equatorial Indian Ocean between $4^0$30'S and $10^0$30'S latitudes. Indian Journal of Marine Science 19, 17-21.

Banerjee, R., Mukhopadhyay, R., 1991. Nature and distribution of manganese nodules from three sediment domains of the Central Indian Basin, Indian Ocean. Geo-Marine Letters 11, 39-43.

Banerjee, R., Roy, S., Dasgupta, S., Mukhopadhyay, S., Miura, H., 1999. Petrogenesis of ferromanganese nodules from east of the Chagos Archipelago, Central Indian Basin, Indian Ocean. Marine Geology 157, 145–158.

Banerjee, R., Devasia, G.K., Ray, D., Balakrishnan, S., 2018. Geochemical, mineralogical, and Sr-Nd isotopic compositions of ferromanganese encrustations from Central Indian Ridge at 06°38.5'S. Geological Journal 53, 2193-2203.

Baturin, G.N., 1988. The geochemistry of manganese and manganese nodules in the ocean. D. Reidel Publishing Company, Dordrecht. 356.

Baturin, G.N., Dubinchuk, V.T., 2011. Mineralogy and Chemistry of Ferromanganese Crusts from the Atlantic Ocean. Geochemical International 49(6), 578-593.

Bau, M., Koschinsky, A., Dulski, P., Hein, J.R., 1996. Comparison of the partitioning behaviours of yttrium, rare earth elements, and titanium between hydrogenetic marine ferromanganese crusts and seawater. Geochimica et Cosmochimica Acta 60(10), 1709-1725.

Bau, M., Schmidt, K., Koschinsky, A., Hein, J.R., Usui, A., 2014. Discriminating between different genetic types of marine ferro-manganese crusts and nodules based on rare earth elements and yttrium. Chemical Geology 381, 1-9.

Blöthe M., Wegorzewski, A. V., Müller, C., Simon, F., Kuhn, T., Schippers, A., 2015. Manganese-cycling microbial communities inside deep-sea manganese nodules. Environmental Science & Technology 49, 7692–7700.

Bodeï, S., Manceau, A., Geoffroy, N., Baronnet, A., Buatier, M., 2007. Formation of todorokite from vernadite in Ni-rich hemipelagic sediments. Geochimica et Cosmochimica Acta 71, 5698–5716.

Bonatti, E., Kraemer, T., Rydell, H., 1972. Classification and genesis of submarine iron-manganese deposits. In: Horn, D. (Ed.), Ferromanganese Deposits on the Ocean Floor, IDOE Publ, Washington, pp. 149-165.

Boström, K., Joensuu, O., Brohm, I., 1974. Plankton: Its chemical composition and its significance as a source of pelagic sediments. Chemical Geology 14, 255–271.

Bruland, K.W., 1983. Trace elements in sea-water. In: J.P. Riley, and R. Chester (Ed.), Chemical Oceanography 8, Academic Press, London, 2nd Ed., 157-220.

Burns, R.G., Bums, V.M., 1979. Manganese oxides. In RG Burns, Ed., Marine Minerals, Reviews in Mineralogy. 6, 1-46.

Burns, R.G., Bums, V.M., Stockman, H.W., 1985. The todorokite-buserite problem: further considerations. American Mineralogists 70, 205-208.

Cronan, D.S., 1980. Underwater Minerals. Academic Press, London, 362 pp.

Dubinin, A.V., 1996. The Formation of Nodules in the Guatemalan Basin Based on the REE Geochemistry Data. Geokhimiya 12, 1210-1219.

Dubinin, A.V., Sval'nov, V.N., 2000a. Geochemistry of Rare Earth Elements in Ferromanganese Micro and Macronodules from the Pacific Nonproductive Zone. Lithology and Mineral Resources 35(6), 520–537.

Dubinin, A.V., Sval'nov, V.N., 2000b.Geochemistry of Rare Earth Elements in Micro and Macronodules from the Pacific Bioproductive Zone. Lithology and Mineral Resources 35(1), 19-31.

Dymond, J., Lyle, M., Finney, B., Piper, D.Z., Murphy, K., Conard, R., Pisias, N., 1984. Ferromanganese nodules from MANOP Sites H, S and R - Control of mineralogical and chemical composition by multiple accretionary processes. Geochimica et Cosmochimica Acta 48, 931-949.

Friedrich, G., Glasby, G.P., Thijssen, T., Plüger, W.L.,1983. Morphological and geochemical characteristics of manganese nodules collected from three areas on an equatorial Pacific transect by R.V. Sonne. Marine Mining 4, 167–253.

Glasby, G.P., 1973. Mechanisms of enrichment of the rarer elements in marine manganese nodules. Marine Chemistry 1(2), 105-125.

Glasby, G.P., 2000. Lesson learned from deep-sea mining. Science 289, 551–553.

González, F.J., Somoza, L., Hein, J.R., Medialdea, T., León, R., Urgorri, V., Reyes, J., Martín-Rubí, J.A., 2016. Phosphorites, Co-rich Mn nodules, and Fe-Mn crusts from Galicia Bank, NE Atlantic: Reflections of Cenozoic tectonics and paleoceanography. Geochemistry, Geophysics, Geosystems 17(2), 346-374.

Halbach, P., Scherhag, C., Hebisch, U., Marchig, V., 1981. Geochemical and Mineralogical Control of Different Genetic Types of Deep-Sea Nodules from the Pacific Ocean. Mineral Deposita 16, 59-84.

Halbach, P., Friedrich, G., Von Stackelberg, U., 1988. The manganese nodule belt of the Pacific Ocean geological environment, nodule formation, and mining aspects. Ferdinand Enke, pp.254.

Heath, G.R., 1981. Ferromanganese nodules of the deep-sea. Economic Geology 75, 736-765.

Hein, J.R., Koschinsky, A., Halbach, P., Manheim, F.T., Bau, M., Kang, J.K., Lubik, N., 1997. Iron and manganese oxide mineralization in the Pacific. In: Nicholson K, Hein JR, Bühn B, Dasgupta S (Ed.) Manganese mineralization: Geochemistry and mineralogy of terrestrial and marine deposits pp. 123-138.

Hein, J.R., Morgan, C.L., 1999. Influence of substrate rocks on Fe–Mn crust composition. Deep-Sea Research I, 46(5), 855-875.

Hein, J.R., Mizell, K., Koschinsky, A., Conrad, T.A., 2013. Deep-ocean mineral deposits as a source of critical metals for high- and green-technology applications: Comparison with land-based resources. Ore Geology Reviews 51, 1-14.

Hein, J.R., Koschinsky, A., 2014. Deep-ocean ferromanganese crusts and nodules. In: Holland, H.D., Turekian, K.K. (Ed.), Treatise on Geochemistry, Second Edition Oxford, Elsevier 13(11), 273-291. DOI: http://dx.doi.org/10.1016/B978-0-08-095975-7.01111-6

Hein, J.R., Spinardi, F., Okamoto, N., Mizell, K., Thorburn, D., Tawake, A., 2015. Critical metals in manganese nodules from the Cook Islands EEZ, abundances and distributions. Ore Geology Reviews 68, 97–116.

Hein, J.R., 2016. Manganese Nodules. In: Harff, J., Meschede, M., Petersen, S., Thiede, J. (Ed.), Encyclopedia of Marine Geosciences. Springer Dordrecht, Heidelberg, New York, London pp. 408-412.

Hein, J.R., Conrad, T.A., Mizell, K., Banakar, V.K., Frey, F.A., Sager, W.W., 2016. Controls on ferromanganese crust composition and reconnaissance resource potential, Ninetyeast Ridge, Indian Ocean. Deep-Sea Research Part I 110, 1-19.

Heller, C., Kuhn, T., Versteegh, G.J.M., Wegorzewski, A.V., Kasten, S., 2018. The geochemical behavior of metals during alteration of manganese nodules buried in deep-sea sediments. Deep Sea Research Part I: Oceanographic Research Papers. DOI: 10.1016/j.dsr.2018.09.008.

Iyer, S.D., Sudhakar, M., 1995. Evidences for a volcanic province in the Central Indian Basin. Journal of the Geological Society of India 46, 353–358.

Jauhari, P., Pattan, J.N., 2000. Ferromanganese nodules from the Central Indian Ocean Basin. Handbook of marine mineral deposits. (Ed.) Cronan, D.S., CRC Press USA pp. 171-195.

Jahauri, P., Iyer, S.D., 2008. A comprehensive view of manganese nodules and volcanics of the Central Indian Ocean Basin. Marine Georesources and Geotechnology 26(4), 231-258.

Josso, P., Pelleter, E., Pourret, O., Fouquet, Y., Etoubleau, J., Cheron, S., Bollinger, C., 2017. A New Discrimination Scheme for Oceanic Ferromanganese Deposits using High Field Strength and Rare Earth Elements. Ore Geology Reviews 87, 3-15.

Kee, N.S., Bloomfield, C., 1961. The solution of some minor element oxides by decomposing plant materials. Geochimica et Cosmochimica Acta 24(3-4), 206-225.

Koschinsky, A., Halbach, P., 1995. Sequential leaching of marine ferromanganese precipitates: genetic implications. Geochimica et Cosmochimica Acta 59, 5113–5132.

Kuhn, T., Bau, M., Blum, N., Halbach, P., 1998. Origin of negative Ce anomalies in mixed hydrothermal–hydrogenetic Fe–Mn crusts from the Central Indian Ridge. Earth and Planetary Science Letters 163, 207-220.

Lyle, M., 1982. Estimating growth rates of ferromanganese nodules from chemical compositions: implications for nodule formation processes. Geochimica et Cosmochimica Acta 46, 2301-2306.

Manceau, A., Gorshkov, A.I., Drits, V.A.,1992. Structural chemistry of Mn, Fe, Co, and Ni in Mn hydrous oxides. II. Information from EXAFS spectroscopy, electron and X-ray diffraction. American Mineralogists 77, 1144–1157.

Manceau, A., Lanson, M., Takahashi, Y., 2014. Mineralogy and crystal chemistry of Mn, Fe Co, Ni, and Cu in a deep-sea Pacific polymetallic nodule. American Mineralogist 99, 2068–2083.

Marino, E., González, F.J., Somoza, L., Lunar, R., Ortega, L., Vázquez, J.T., Reyes, J., Bellidoa, E., 2017. Strategic and rare elements in Cretaceous-Cenozoic cobalt-rich ferromanganese crusts from seamounts in the Canary Island Seamount Province (northeastern tropical Atlantic). Ore Geology Reviews 87, 41–61.

Marino, E., González, F.J., Lunar, R., Reyes, J., Medialdea, T., Castillo-Carrión, M., Bellidoa, E., Somoza, L., 2018. High-Resolution Analysis of Critical Minerals and Elements in Fe–Mn Crusts from the Canary Island Seamount Province (Atlantic Ocean). Minerals 8, 285, doi:10.3390/min8070285.

Mero, J.L., 1965. Mineral Resources of the Sea. Elsevier, Amsterdam. 312 pp.

Moffett, J.W.,1990. Microbially mediated cerium oxidation in seawater. Nature 345, 421-423.

Mohwinkel, D., Kleint, C., Koschinsky, A., 2014. Phase associations and potential selective extraction methods for selected high-tech metals from ferromanganese nodules and crusts with siderophores. Applied Geochemistry 43, 13–21.

Muiños, S.B., Hein, J.R., Frank, M., Monteiro, J.H., Gaspar, L., Conrad, T., Pereira, H.G., Abrantes, F., 2013. Deep-sea Fe-Mn Crusts from the Northeast Atlantic Ocean: Composition and Resource Considerations. Marine Georesources and Geotechnology 31(1), 40-70. DOI: 10.1080/1064119X.2012.661215.

Mukhopadhyay, R., Ghosh, A.K., Iyer, S.D., 2008. The Indian Ocean nodule field: Geology and resource potential. Handbook Exploration Environ Geochem10 (Ed.), Hale, M., Elsevier; Amsterdam; The Netherlands.

Murphy, K., Dymond, J., 1984. Rare Earth Element Fluxes and Geochemical Budget in the Eastern Equatorial Pacific. Nature (London) 307(5950), 444-447.

Nath, B.N., Rao, V.P., Becker, K.P., 1989. Geochemical evidence of terrigenous influence in deep-sea sediments up to 8°S in the Central Indian Basin. Marine Geology 87, 301-313.

Ohta, A., Ishii, S., Sakakibara, M., Mizuno, A., Kawabe, I., 1999. Systematic correlation of the Ce anomaly with the Co/(Ni+Cu) ratio and Y fractionation from Ho in distinct types of Pacific deep-sea nodules. Geochemical Journal 33, 399-417.

Ohta, A., Kawabe, I., 2001. REE(III) adsorption onto Mn dioxide (δ-MnO_2) and Fe oxyhydroxide: Ce(III) oxidation by δ-MnO_2. Geochimica et Cosmochimica Acta 65(5), 695-703.

Ostwald, J., 1984. Ferruginous vernadite in an Indian Ocean ferromanganese nodule. Geological Magazine 121(5), 483-488.

Pakarinen, J., Koivula, R., Laatikainen, M., Laatikainen, K., Paatero, E., Harjula, R., 2010. Nanoporous manganese oxides as environmental protective materials—Effect of Ca and Mg on metals sorption. Journal of Hazardous Materials 180, 234–240.

Pattan, J.N., Banakar, V.K., 1993. Rare earth element distribution and behaviour in buried managanese nodules from the Central India Basin. Marine Geology112, 303-312.

Pattan, J.N., Parthiban, G., 2011. Geochemistry of ferromanganese nodule–sediment pairs from Central Indian Ocean Basin. Journal of Asian Earth Science 40, 569–580.

Pelleter, E., Fouquet, Y., Etoubleau, J., Cheron, S., Labanieh, S., Josso, P., Langlade, J., 2017. Ni-Cu-Co-rich hydrothermal manganese mineralization in the Wallis and Futuna back-arc environment (SW Pacific). Ore Geology Reviews 87, 126-146.

Post, J.E., Bish, D.L., 1988. Rietveld refinement of the todorokite structure. American Mineralogist 73, 861–869.

Price, N.B., 1967. Some geochemical observations on manganese-iron oxide nodules from different depth environments. Marine Geology 5, 511-538.

Price, N.B., Calvert, S.E., 1970. Compositional variation in Pacific Ocean ferromanganese nodules and its relationship to sediment accumulation rates. Marine Geology 9, 145-171.

Rona, P.A., 2008. The changing vision of marine minerals. Ore Geology Reviews, 33, 618-666.

Schmidt, K., Bau, M., Hein, J., Koschinsky, A., 2014. Fractionation of the geochemical twins Zr-Hf and Nb-Ta during scavenging from seawater by hydrogenetic ferromanganese crusts. Geochimica et Cosmochimica Acta 140, 468-487.

Schnetger, B., 1992. Chemical composition of loess from a local and worldwide view. Neues Jahrbuch der Mineralogie 1, 29–47.

Scott, S.D., Atmanand, M.A., Hein, J., Heydon, D., Morgan, C., 2006. Engineering Committee on Ocean Resources. Mineral deposits in the sea: a future resource symposium. Report, Specialist Panel on Marine Mining. 13 pp.

Sensarma, S., Chakraborty, P., Banerjee, R., Mukhopadhyay, S., 2016. Geochemical fractionation of Ni, Cu and Pb in the deep sea sediments from the Central Indian Ocean Basin: An insight into the mechanism of metal enrichment in sediment. Geochemistry 76(1), 39-48.

Sensarma, S., Banerjee, R., Satyanarayanan, M., Mukhopadhyay, S., 2018. Depositional environment of the surface sediments in Central Indian Basin (CIB), Indian Ocean, between 8°–18°S latitude and 72°–79°E longitude, based on their geochemical characteristics. Geological Journal, 53, 1586–1603.

Sholkovitz, E.R., Landing, W.M., Lewis, B.L., 1994. Ocean Particle Chemistry: The Fractionation of Rare Earth Elements between Suspended Particles and Seawater. Geochimica et Cosmochimica Acta 58(6), 1567-1579.

Takahashi, Y., Manceau, A., Geoffroy, N., Marcus, M.A., Usui, A., 2007. Chemical and structural control of the partitioning of Co, Ce, and Pb in marine ferromanganese oxides. Geochimica et Cosmochimica Acta 71(4), 984-1008.

Takematsu, N., Sato, Y., Okabe, S., 1989. Mechanisms of incorporation of rare earth elements into ferromanganese concretions. La mer 27, 41-52.

Wegorzewski, A.V., Kuhn, T., 2014. The influence of suboxic diagenesis on the formation of manganese nodules in the Clarion Clipperton nodule belt of the Pacific Ocean. Marine Geology 357, 123–138.

Wegorzewski, A.V., Grangeon, S., Webb, S.M., Heller, C., Kuhn, T., 2020. Mineralogical transformations in polymetallic nodules and the change of Ni, Cu and Co crystal-chemistry upon burial in sediments. Geochimica et Cosmochimica Acta 282, 19-37.

Wehausen, R., Brumsack, H.J., 1999. Cyclic variations in the chemical composition of eastern Mediterranean Pliocene sediments: A key for understanding sapropel formation. Marine Geology 153, 161–176.

Wu, Z., Peacock, C.L., Lanson, B., Yin, H., Zheng, L., Chen, Z., Tan, W., Qiu, G., Liu, F., Feng, X., 2019. Transformation of Cocontaining birnessite to todorokite: Effect of Co on the transformation and implications for Co mobility. Geochimica et Cosmochimica Acta 246, 21–40.

Table captions:

- **Table 1:** Locations, sediment type, Fe, Mn concentrations, Mn/Fe ratio, genetic type and growth rates (in mm/10^6years) of the nodule samples under study.
- **Table 2:** Trace and Rare Earth element concentrations of the nodule samples under study; concentrations are in ppm unless stated otherwise.
- **Table 3:** EPMA results of the average elemental concentrations in wt% for selected nodule samples (for detailed explanations see text).
- **Table 4:** Few important parameters of the nodule samples under study according to their sediment type. Average values of all elemental concentrations and growth rates are mentioned.
- **Table 5:** Compiled data of morphological settings of the different sediment types in CIOB (after Iyer and Sudhakar, 1995; Jauhari and Iyer, 2008).
- **Table 6:** Correlation coefficient matrix of nodules from (a) siliceous sediment (n = 21), (b) siliceous-red clay transition sediment (n = 7) and (c) red clay sediment (n = 7). ΣREY is in ppm, rest all are in wt%. Values in bold have confidence level >99.9%.

Figure captions:

- **Figure 1:** Distribution of nodule samples in the study area within CIOB along with depth contour of the area. The sediment type demarcation is according to Nath et al. (1989).
- **Figure 2:** Morphological variation of nodules from (a) siliceous sediment, (b) siliceous-red clay transition zone sediment and (c) red clay sediment in the present study. The scale of dimension is in centimeter.
- **Figure 3:** Mineralogical variation of nodules from (a) siliceous sediment, (b) siliceous-red clay transition zone sediment and (c) red clay sediment. T = todorokite, Q = quartz, Al = albite, An = anorthite, V = vernadite and No = nontronite.
- **Figure 4:** Back Scattered Electron (BSE) EPMA image of microlayers in nodules viz. (a) core to rim variation with alternate Fe and Mn-rich layers; (b) an equant shaped plagioclase grain in the core with colloidal Mn-rich layers around it; (c) core to rim variation; (d) overgrowth of Fe-Mn hydroxide layers over shark tooth in core; (e) weathered basalt in the core, surrounded by globular Mn-rich layers and (f) presence of fish tooth and Mn-rich material in the core of a nodule, around which alternate Mn/Fe-rich and Si-rich layers grew.
- **Figure 5:** Regression relation between Mn/Fe ratio of the selected nodule microlayers with their (a) Cu, (b) Ni and (c) Co concentrations. Copper and nickel show positive relation (R = 0.74 and 0.60 respectively) whereas, cobalt shows negative relation (R = -0.35) for n = 20.
- **Figure 6:** Ternary diagram showing the relationship between geochemistry and different genetic types of the nodules (as per Halbach et al., 1981).
- **Figure 7:** Ternary diagram representing the relationship between major, HFSE and REE data with different genetic types of the nodules (as per Josso et al., 2017). The dotted arrows present the mixing trends between two genetic processes highlighting the existing continuum. Solid arrows show evolution trends of a sample set related to only one genetic process without influence of another one.
- **Figure 8:** (a) Ce/Ce* vs. Nd and (b) Ce/Ce*vs. Y_N/Ho_N plots (as per Bau et al., 2014) show all the nodules from present study falling in the hydrogenetic-mixed field. For explanation see text.
- **Figure 9:** Post Achaean Australian Shale normalized REE pattern of nodules (averaged) according to (a) different sediment types and (b) genetic types. For explanation see text.
- **Figure 10:** A schematic representation of the nodule formation process and their subsequent growth in different sediment types. The red arrows indicate metal incorporation from oxic bottom water i.e., hydrogenetic source, whereas green arrows indicate early diagenetic source. The width of the green arrows changes according to sediment type indicating the strength of metal influx through sediment pore water.

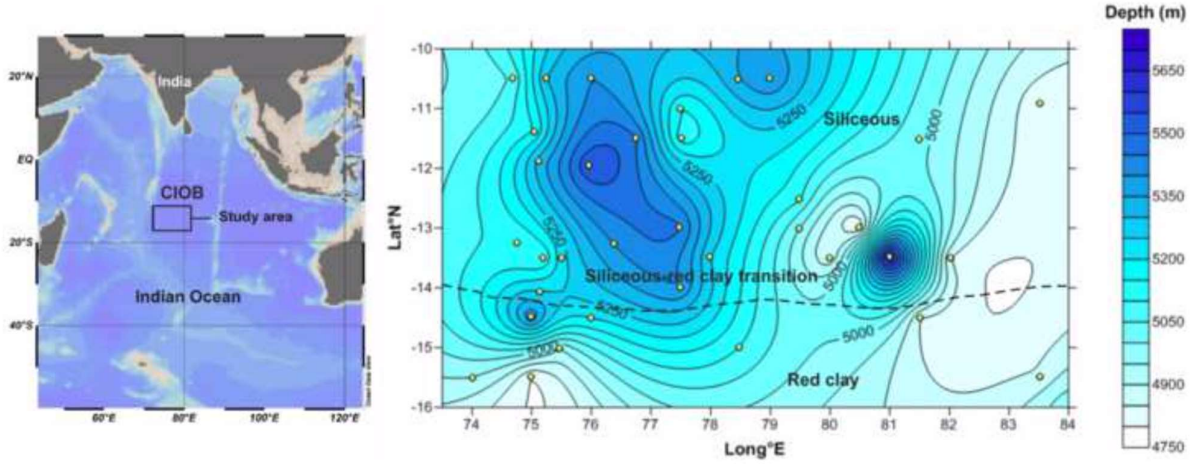

Figure 1

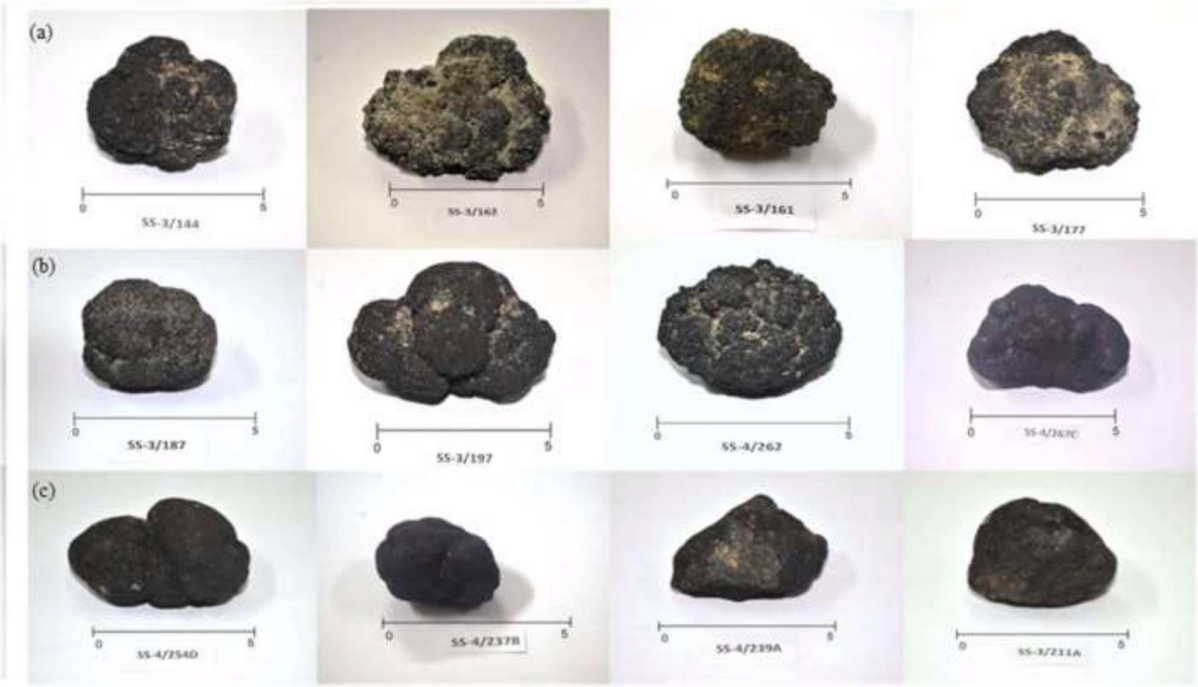

Fig.2

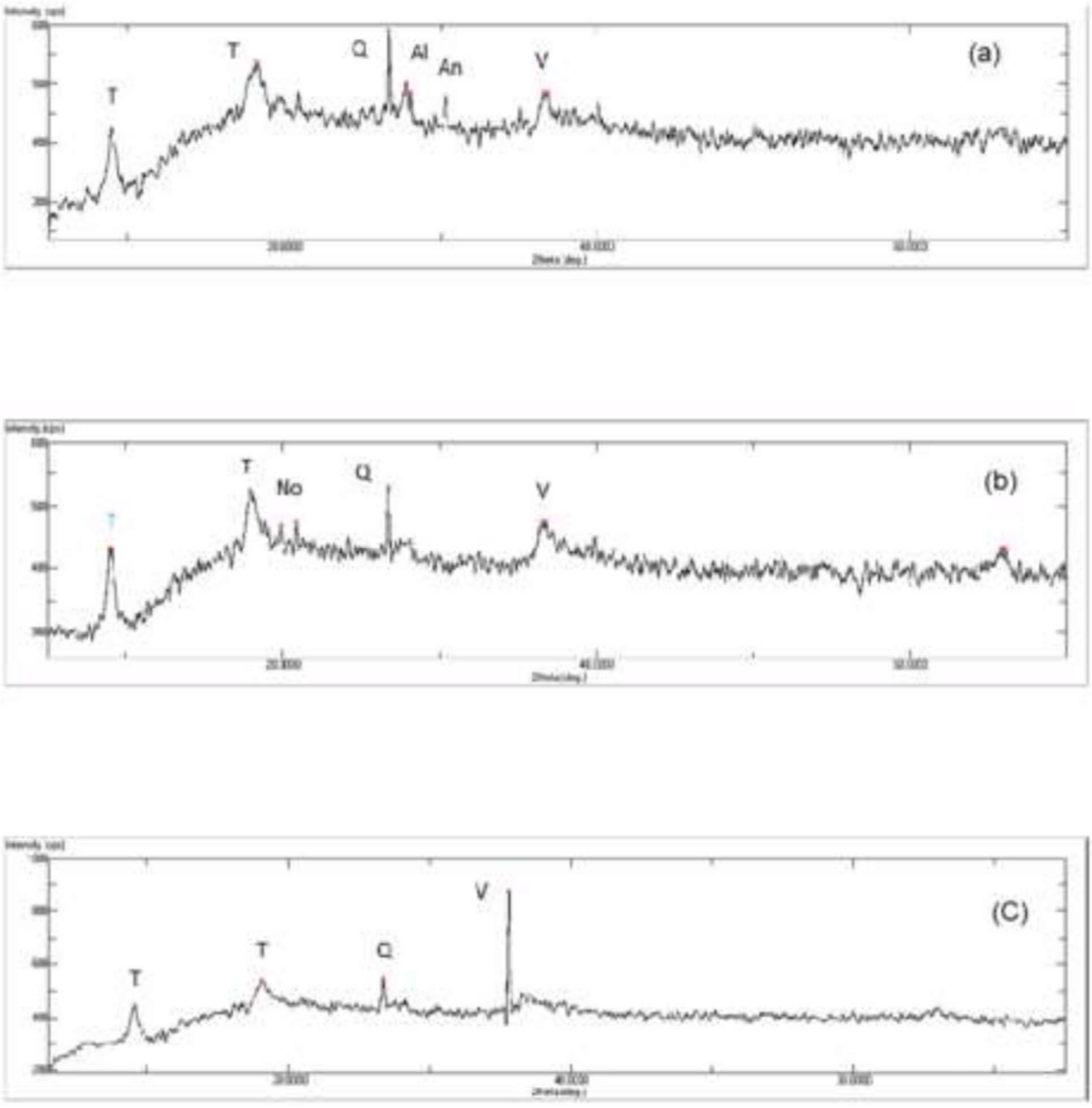

Figure 3

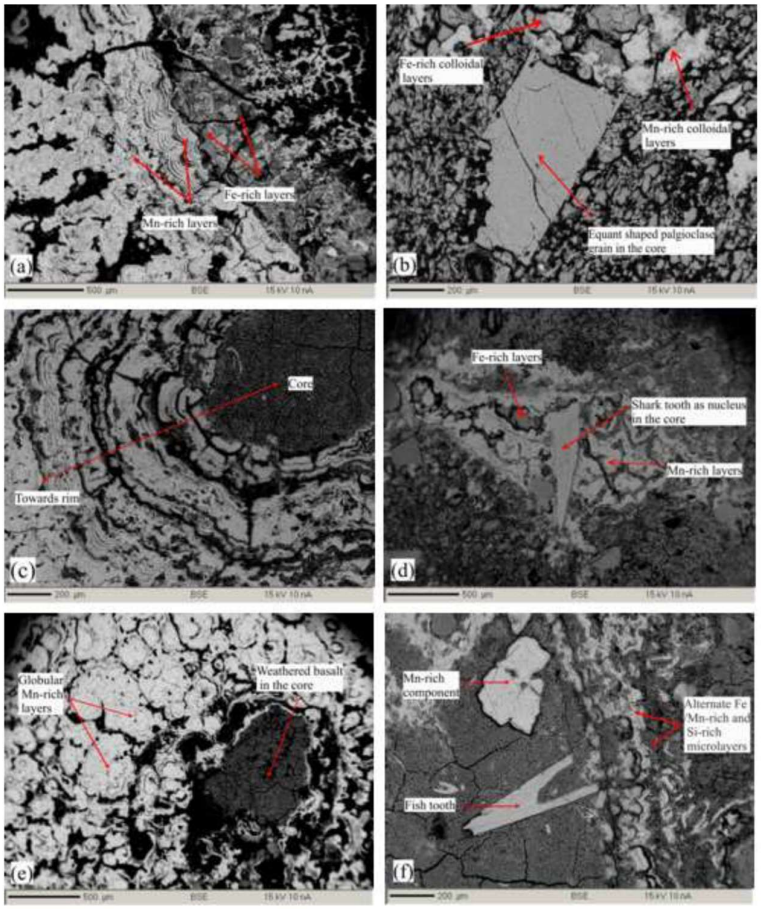
Fe-rich layers
Mn-rich layers
(a)
Fe-rich colloidal layers
Mn-rich colloidal layers
Equant shaped palgioclase grain in the core
(b)
Core
Towards rim
(c)
Fe-rich layers
Shark tooth as nucleus in the core
Mn-rich layers
(d)
Globular Mn-rich layers
Weathered basalt in the core
(e)
Mn-rich component
Alternate Fe Mn-rich and Si-rich microlayers
Fish tooth
(f)

Figure 4

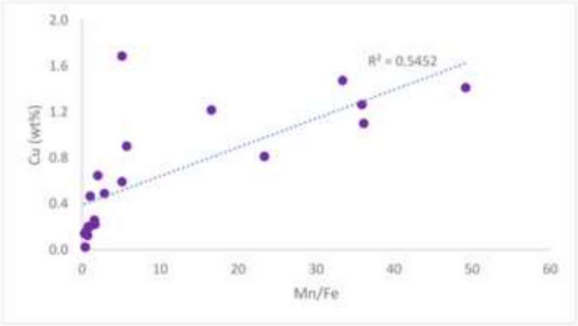
2.0
1.6
1.2
0.8
0.4
0.0
Cu (wt%)
R² = 0.5452
0
10
20
30
40
50
60
Mn/Fe

(a)

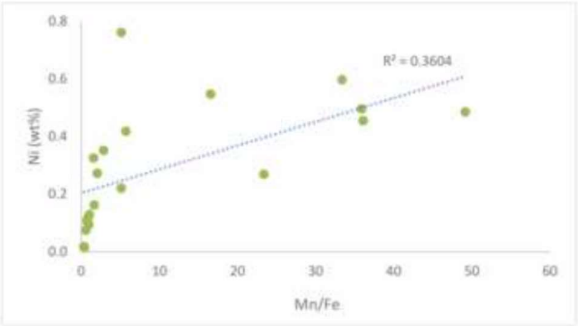
0.8
0.6
0.4
0.2
0.0
Ni (wt%)
R² = 0.3604
0
10
20
30
40
50
60
Mn/Fe

(b)

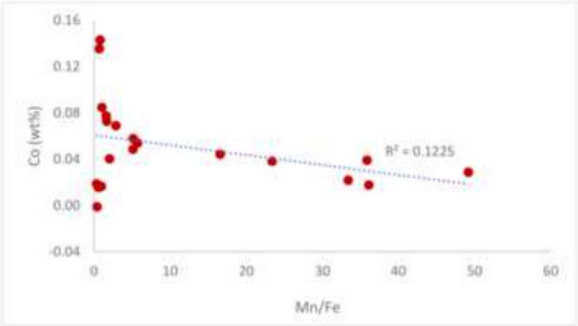
0.16
0.12
0.08
0.04
0.00
-0.04
Co (wt%)
R² = 0.1225
0
10
20
30
40
50
60
Mn/Fe

(c)

Figure 5

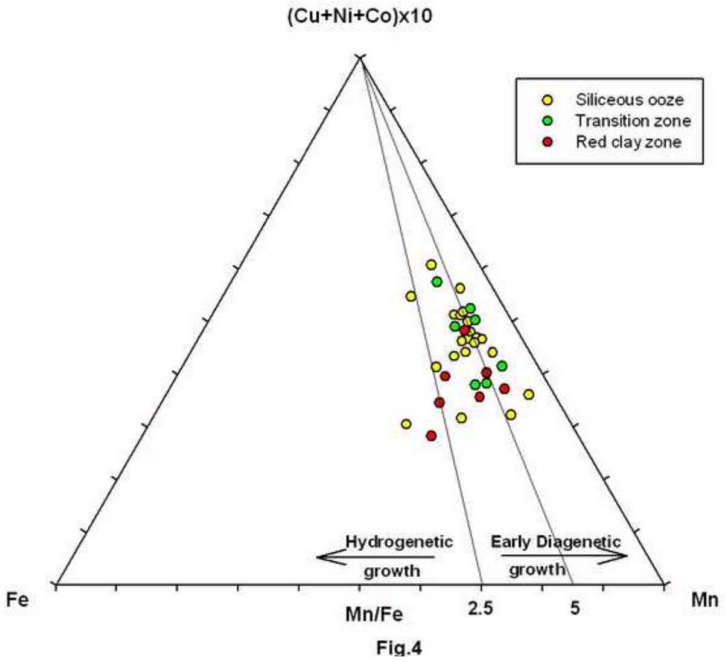

Figure 6

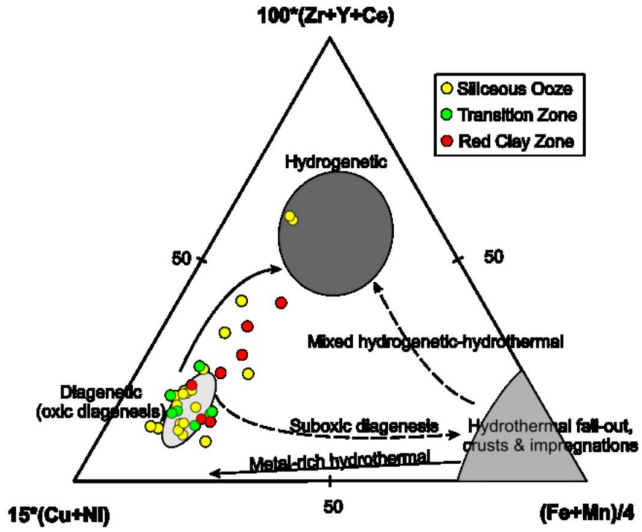

Figure 7

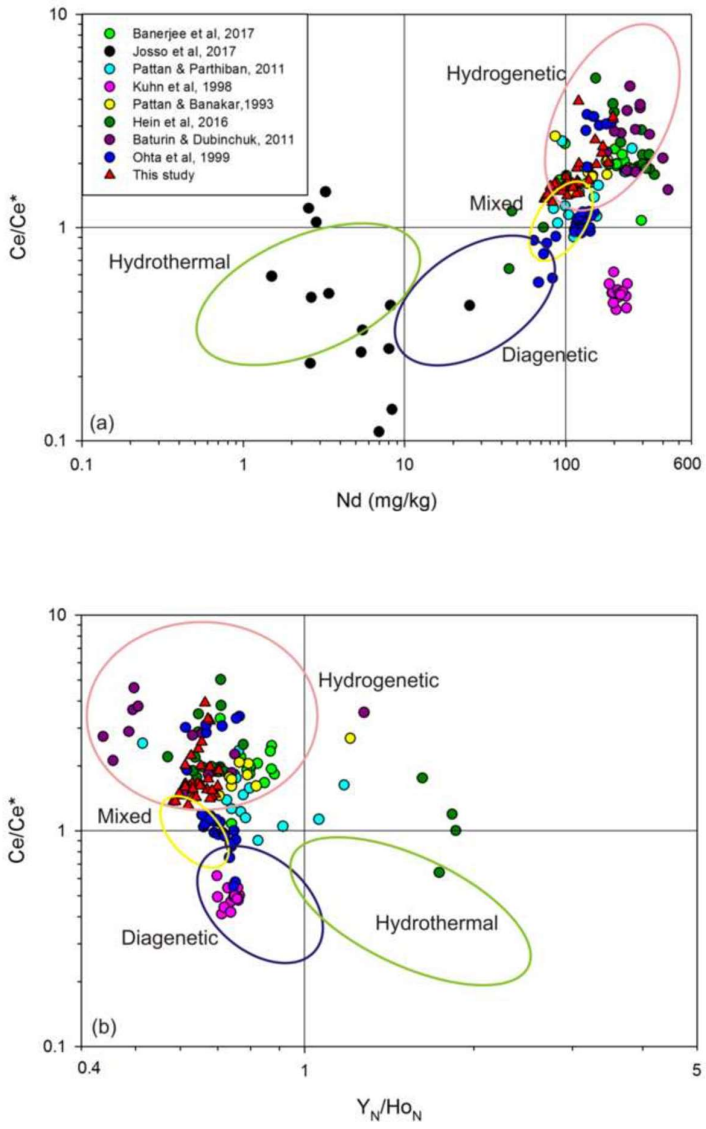
Banerjee et al, 2017
Josso et al, 2017
Pattan & Parthiban, 2011
Kuhn et al, 1998
Pattan & Banakar,1993
Hein et al, 2016
Baturin & Dubinchuk, 2011
Ohta et al, 1999
This study
Hydrogenetic
Mixed
Hydrothermal
Diagenetic
(a)
Ce/Ce*
Nd (mg/kg)
10
1
0.1
0.1
1
10
100
600
Hydrogenetic
Mixed
Diagenetic
Hydrothermal
(b)
Ce/Ce*
Y_N/Ho_N
10
1
0.1
0.4
1
5

Figure 8

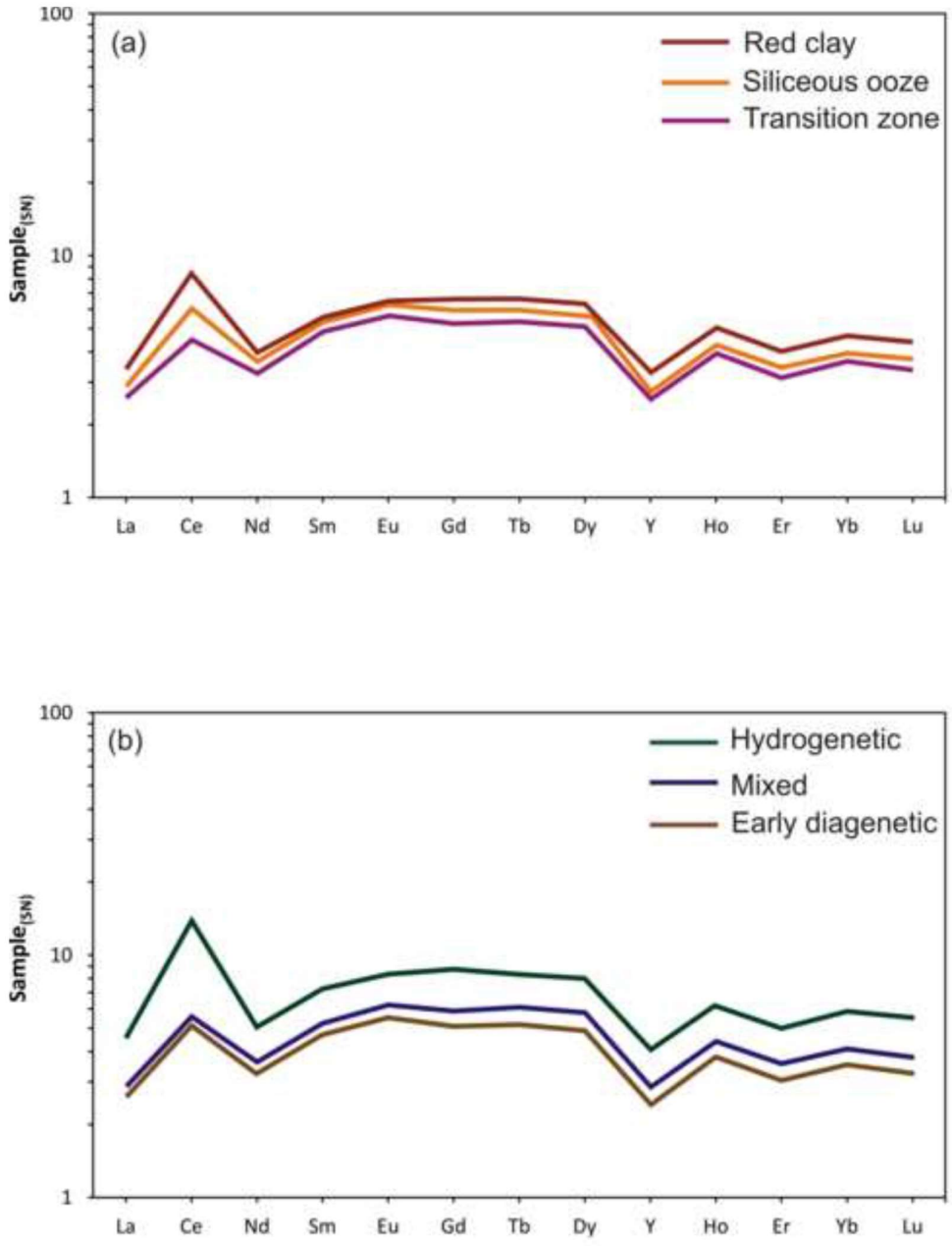

Figure 9

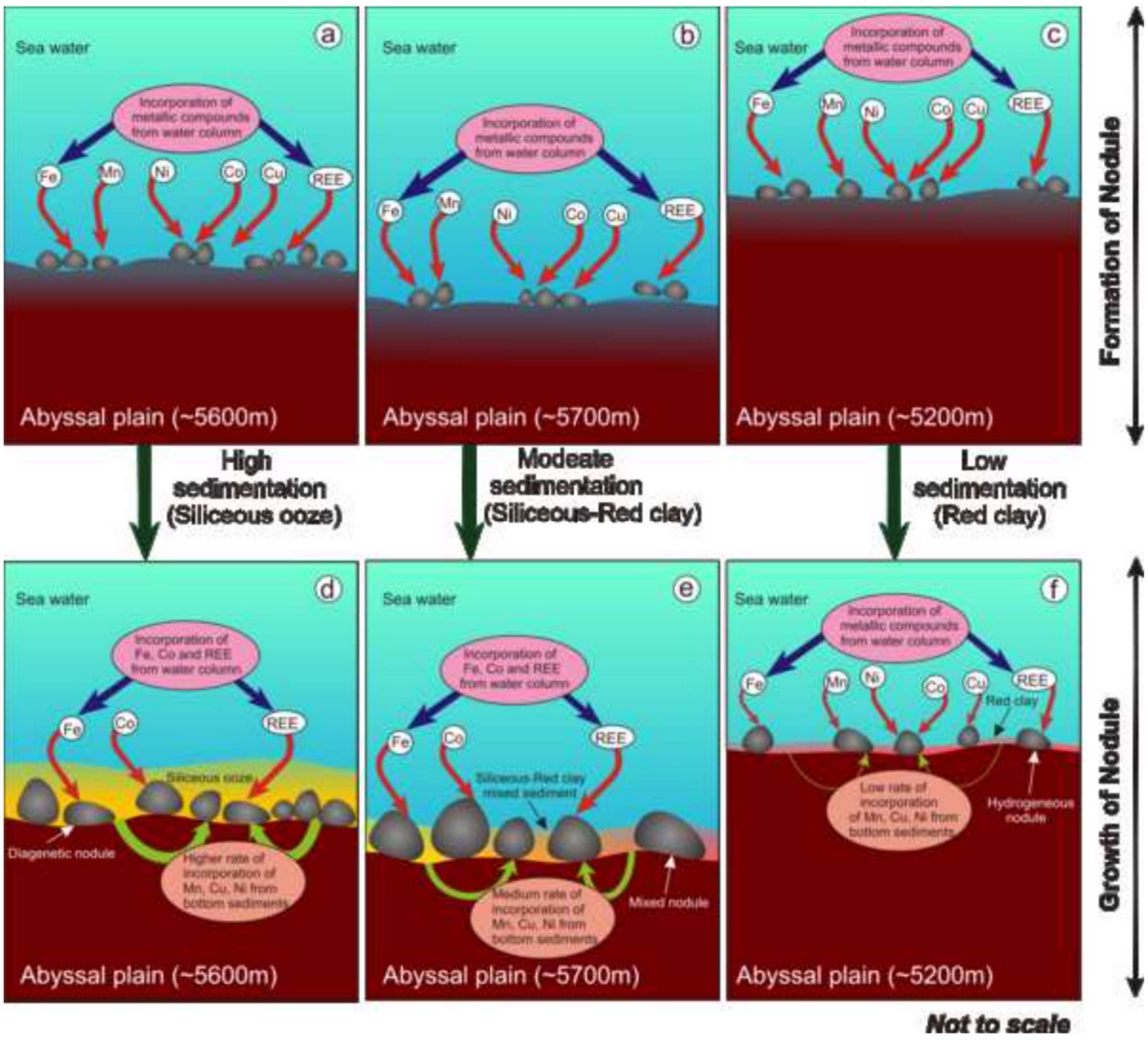
a
b
c
Sea water
Incorporation of metallic compounds from water column
Fe
Mn
Ni
Co
Cu
REE
Abyssal plain (~5600m)
Abyssal plain (~5700m)
Abyssal plain (~5200m)
Formation of Nodule
High sedimentation (Siliceous ooze)
Modeate sedimentation (Siliceous-Red clay)
Low sedimentation (Red clay)
d
e
f
Incorporation of Fe, Co and REE from water column
Siliceous ooze
Diagenetic nodule
Higher rate of incorporation of Mn, Cu, Ni from bottom sediments
Siliceous-Red clay mixed sediment
Medium rate of incorporation of Mn, Cu, Ni from bottom sediments
Mixed nodule
Red clay
Low rate of incorporation of Mn, Cu, Ni from bottom sediments
Hydrogeneous nodule
Growth of Nodule
Not to scale

Figure 10

List of Tables

Table 1: Locations, sediment type, Fe, Mn concentrations, Mn/Fe ratio, genetic type and growth rates (in mm/10^6years) of the nodule samples under study.

Sr. No.	Sample	Lat°S	Long°E	Depth(m)	Sediment type	Fe%	Mn%	Mn/Fe	Genetic type	Growth rate	Main Mineral
1	283	10.50	75.24	5300	Siliceous	5.70	19.42	3.41	Mixed	10.03	Todorokite
2	285	10.50	74.69	5058	"	7.78	16.85	2.17	"	4.90	"
3	217A	10.50	75.99	5400	"	4.16	24.45	5.88	Diagenetic	23.06	"
4	428A	10.50	78.98	5400	"	3.74	20.91	5.59	"	24.31	"
5	133E	10.52	78.46	5345	"	4.81	29.6	6.15	"	20.92	"
6	144	10.92	83.51	4815	"	5.84	29.11	4.98	Mixed	14.10	"
7	161	11.00	77.50	5150	"	3.99	32.06	8.04	Diagenetic	32.64	"
8	291	11.38	75.05	5150	"	7.34	18.30	2.49	Mixed	5.88	"
9	162	11.49	77.51	5120	"	3.27	45.85	14.02	Diagenetic	68.89	"
10	318F	11.50	76.75	5459	"	2.84	19.98	7.04	"	40.18	"
11	139	11.51	81.48	5020	"	10.17	29.49	2.90	Hydrogenetic	5.01	Both
12	301	11.88	75.12	5320	"	5.12	21.96	4.29	Mixed	13.83	Todorokite
13	87	11.95	75.95	5544	"	3.97	22.52	5.67	Diagenetic	23.32	"
14	190A	12.51	79.48	5112	"	4.83	26.73	5.53	"	18.76	"
15	177	12.99	77.47	5460	"	4.18	29.45	7.05	"	27.39	"
16	275B	12.99	80.49	4800	"	6.70	28.44	4.24	Mixed	10.57	"
17	467	13.01	79.49	5000	"	4.46	19.98	4.48	"	16.50	"
18	309	13.24	74.75	5107	"	3.41	21.96	6.44	Diagenetic	30.69	"
19	317	13.26	76.37	5400	"	10.83	16.89	1.56	Hydrogenetic	2.75	"
20	321	13.50	75.19	5100	"	4.53	23.41	5.17	Diagenetic	18.70	"
21	319	13.50	75.50	5230	"	3.79	14.95	3.94	Mixed	17.10	"
22	262	13.49	77.98	5250	Sili-Red clay	5.24	21.73	4.15	"	13.13	"
23	267C	13.49	80.99	5700	"	4.38	17.26	3.94	"	14.82	Vernadite

24	197	13.51	82.01	4848	"	6.16	31.43	5.10	"	13.72	Todorokite
25	187	13.51	80.00	4860	"	4.24	37.17	8.77	Diagenetic	33.55	"
26	260F	13.99	77.49	5400	"	3.24	23.97	7.40	"	36.98	"
27	325	14.06	75.13	5250	"	3.34	24.31	7.28	"	35.28	"
28	225A	14.49	74.99	5400	"	6.67	27.36	4.10	Mixed	10.29	"
29	541B	14.51	75.99	5200	Red clay	3.77	18.68	4.95	"	21.50	"
30	201F	14.50	81.50	4848	"	5.26	37.46	7.12	"	22.13	Vernadite
31	254D	14.99	78.48	5100	"	6.62	27.29	4.12	"	10.41	"
32	235E	15.02	75.47	4950	"	8.84	23.97	2.71	"	5.36	Todorokite
33	237B	15.49	74.99	4800	"	5.55	30.87	5.56	Diagenetic	16.48	"
34	211A	15.49	83.51	4860	"	10.79	21.17	1.96	Hydrogenetic	3.36	Both
35	239A	15.50	74.00	4950	"	10.11	23.52	2.33	"	4.13	"

Table 2: Trace and Rare Earth element concentrations of the nodule samples under study; concentrations are in ppm unless stated otherwise.

Sample	**Co %**	**Ni %**	**Cu %**	**Zr**	**La**	**Ce**	**Nd**	**Sm**	**Eu**	**Gd**	**Tb**	**Dy**	**Y**	**Ho**	**Er**	**Yb**	**Lu**	**∑REY**
283	0.14	0.92	0.86	1080	128.5	492.3	138.7	34.90	8.02	32.40	5.43	29.40	88.57	5.09	11.74	12.69	1.82	1382.3
285	0.10	1.61	1.25	743.7	93.02	356.8	105.0	27.90	6.44	24.52	4.34	22.85	65.83	3.99	9.29	10.68	1.52	1033.5
217A	0.14	1.31	1.40	733.0	112.1	366.3	116.2	29.13	6.77	26.94	4.52	24.69	82.65	4.48	10.20	11.28	1.58	1129.9
428A	0.11	1.03	1.13	609.0	89.49	320.2	96.37	24.69	5.58	22.37	3.82	19.97	64.18	3.55	8.26	9.10	1.29	939.16
133E	0.08	1.62	1.32	440.8	74.94	288.2	87.93	23.41	5.46	20.59	3.52	18.93	53.97	3.28	7.83	8.94	1.26	846.07
144	0.12	1.53	1.40	272.0	108.9	369.0	120.9	32.20	7.45	27.96	4.85	25.62	72.68	4.48	10.11	11.54	1.57	1143.6
161	0.07	1.49	1.27	336.1	64.27	209.1	75.19	19.81	4.59	16.75	2.83	14.81	40.65	2.56	5.99	6.85	0.99	676.86
291	0.18	0.87	0.75	1145	175.0	859.0	167.0	41.45	9.38	39.58	6.30	33.04	100.1	5.91	13.38	14.92	2.05	1959.8
162	0.06	1.43	1.27	273.1	61.75	201.8	73.56	19.88	4.67	16.77	2.83	15.33	42.60	2.71	6.28	7.13	1.00	663.60
318F	0.09	1.32	1.51	375.6	69.05	229.1	76.44	20.53	4.77	17.92	3.09	16.58	48.18	2.83	6.58	7.48	1.02	722.87

139	0.20	1.04	0.59	193.2	173.0	795.8	183.2	47.56	10.74	43.99	7.15	37.80	108.5	6.56	14.81	16.26	2.28	1976.6
301	0.10	1.26	0.96	861.2	109.3	415.8	117.5	30.55	6.95	27.14	4.76	24.98	74.51	4.38	10.11	11.17	1.61	1177.1
87	0.10	1.39	1.35	577.1	92.22	344.8	101.3	27.48	6.11	23.88	4.12	21.96	65.48	3.89	9.02	10.13	1.42	1000.3
190A	0.12	1.25	1.30	322.9	89.21	302.7	95.09	24.45	5.71	21.77	3.74	20.30	66.76	3.57	8.44	9.40	1.36	916.80
177	0.09	1.37	1.47	351.9	74.66	259.0	83.85	22.25	5.12	19.02	3.26	17.77	49.69	3.08	7.16	8.35	1.17	792.44
275B	0.19	1.30	1.28	345.0	123.6	515.2	116.6	29.12	6.79	28.87	4.75	26.03	87.53	4.61	10.73	11.90	1.69	1302.7
467	0.12	1.27	1.17	662.9	98.61	355.0	108.0	27.84	6.60	24.84	4.21	22.53	68.31	4.01	9.23	10.53	1.46	1051.0
309	0.23	0.60	0.37	1482	205.6	1494	195.6	49.74	11.30	49.62	7.84	41.66	134.7	7.42	17.18	19.25	2.79	2806.0
317	0.24	0.60	0.37	1491	204.2	1454	195.8	48.67	11.11	50.28	7.69	41.35	135.0	7.37	16.97	19.16	2.75	2759.8
321	0.12	1.36	1.44	696.4	114.2	421.4	120.9	30.79	7.06	28.14	4.83	25.46	79.59	4.50	10.63	11.70	1.66	1203.9
319	0.08	1.31	1.49	376.8	70.34	232.9	77.20	20.53	4.79	17.44	3.04	16.57	48.19	2.79	6.47	7.35	1.02	732.91
262	0.15	1.27	1.16	900.8	115.7	525.8	120.7	30.81	7.00	29.03	4.85	26.26	82.49	4.68	10.76	11.92	1.72	1317.5
267C	0.10	1.59	1.22	721.3	90.78	351.3	103.2	27.90	6.31	24.35	4.21	22.57	64.57	3.90	9.19	10.39	1.47	1016.0
197	0.14	1.10	1.08	242.8	119.4	430.0	118.4	29.49	6.88	28.03	4.67	25.30	78.75	4.48	10.25	11.62	1.64	1209.5
187	0.13	1.35	1.45	381.2	92.14	301.7	101.7	26.11	5.98	22.91	3.93	21.12	67.48	3.69	8.56	9.67	1.31	949.80
260F	0.08	1.24	1.42	598.1	75.57	229.7	82.5	21.59	4.95	18.21	3.13	17.01	48.86	2.92	6.84	7.73	1.11	753.74
325	0.08	1.48	1.47	589.9	74.66	280.6	85.07	23.36	5.41	20.38	3.42	18.53	51.78	3.13	7.46	8.59	1.22	828.56
225A	0.13	1.01	0.93	226.0	107.8	391.1	109.9	27.91	6.20	25.91	4.29	23.22	79.27	4.20	9.67	10.32	1.50	1117.6
541B	0.06	1.12	0.91	678.1	73.29	265.1	80.01	20.74	4.89	19.22	3.24	17.44	53.76	3.15	7.17	8.10	1.15	786.69
201F	0.13	1.16	1.23	267.7	106.9	372.2	110.2	27.59	6.49	25.84	4.45	23.95	79.30	4.30	9.97	10.95	1.56	1094.2
254D	0.19	0.97	0.71	761.3	176.2	933.6	169.8	41.96	9.43	40.76	6.54	35.72	112.1	6.42	14.89	16.34	2.32	2054.0
235E	0.17	0.99	0.98	409.1	158.8	693.5	154.5	38.77	8.83	38.36	6.26	34.56	114.1	6.24	14.76	16.32	2.38	1730.9
237B	0.13	1.10	1.22	252.1	100.7	391.3	100.3	25.54	5.85	24.19	4.04	22.45	73.30	4.03	9.37	10.48	1.47	1065.2
211A	0.22	0.58	0.45	276.3	147.3	1203	119.8	28.83	6.68	33.32	5.10	28.55	98.25	5.48	13.26	15.75	2.40	2067.3
239A	0.17	0.94	0.66	310.1	152.9	879.9	151.7	37.61	8.38	36.38	5.93	31.76	99.95	5.65	13.01	14.55	2.07	1878.3

Table 3: EPMA results of the average elemental concentrations in wt% for selected nodule samples (for detailed explanations see text).

Sl. No.	No. of points	Al	Si	Mn	Fe	Co	Ni	Cu
1	19	12.53	19.32	0.81	0.86	0.00	0.02	0.02
2	18	4.20	10.54	19.82	6.17	0.02	0.46	1.10
3	14	1.54	1.43	24.80	2.43	0.02	0.60	1.48
4	15	2.84	7.18	22.83	7.39	0.03	0.49	1.41
5	10	7.78	19.35	5.28	4.85	0.02	0.07	0.16
6	17	6.40	10.70	15.42	5.48	0.04	0.27	0.65
7	35	3.22	4.46	24.29	5.85	0.06	0.76	1.69
8	18	4.70	10.38	18.52	9.09	0.08	0.33	0.26
9	33	3.22	6.58	19.51	8.75	0.07	0.35	0.49
10	32	4.37	9.04	8.81	7.80	0.14	0.11	0.12
11	21	5.78	9.66	12.29	12.58	0.14	0.12	0.20
12	10	4.82	7.25	13.99	8.59	0.07	0.16	0.22
13	25	6.73	17.25	4.30	10.96	0.02	0.02	0.14
14	20	5.83	8.59	16.97	3.79	0.05	0.42	0.90
15	30	4.93	10.92	16.21	11.87	0.05	0.22	0.59
16	35	3.26	13.61	6.56	5.04	0.02	0.09	0.20
17	25	5.51	10.98	14.46	4.87	0.04	0.27	0.81
18	34	3.95	3.13	24.70	2.43	0.04	0.50	1.26
19	28	4.74	9.65	14.56	12.17	0.08	0.13	0.47
20	47	2.62	3.05	22.82	2.49	0.04	0.55	1.22

Table 4: Few important parameters of the nodule samples under study according to their sediment type. Average values of all elemental concentrations and growth rates are mentioned.

	Siliceous	**Siliceous-Red clay**	**Pelagic red clay**
Water depth (m)	5204.3	5244	4958.3
Long axis dimension (cm)	4	5	4
Percentage in total population	60	20	20
Predominant shape	Sub-rounded, ellipsoidal, globular, elongate, irregular	Sub-rounded, ellipsoidal, globular, elongate	Sub-rounded, elongate
Surface texture	Rough	Rough	Smooth
Nature of nodules	Mono and poly-nucleated	Mono and poly-nucleated	Mono and poly-nucleated
Relative density	Very light to heavy	Very light to heavy	light to heavy
Oxide layer thickness (mm)	1-3	1-3	0.5-2
Mineralogy	Todorokite, Vernadite, Quartz, Albite, Anorthoclase,	Todorokite, Vernadite, Quartz, Nontronite, Albite, Anorthoclase	Vernadite, Todorokite, Quartz, Albite
Growth rate	18.03mm/10^6yrs	22.54mm/10^6yrs	11.91mm/10^6yrs
Mn %	24.40	26.18	26.14
Fe %	5.31	4.75	7.28
Ni %	1.23	1.29	0.98
Cu %	1.14	1.25	0.88
Co %	0.13	0.12	0.15
Zr (mg/kg)	636.60	522.87	422.10
Mn/Fe	5.29	5.82	4.11
Ni+Cu+Co %	2.50	2.65	2.01
∑REE (mg/kg)	1248.43	997.41	1648.31

Table 5: Compiled data of morphological settings of the different sediment types in CIOB (after Iyer and Sudhakar, 1995; Jauhari and Iyer, 2008).

Areas Sediment type	**General description**	**Morpho-tectonics**	**Nuclei for nodules**	**Nodule characters**	**Volcanic weathered material**
Area 1 Terrigenous	Influence of Ganges-Brahmaputra rivers, rapid sedimentation leading to burial of nodule nuclei	Absence of seamounts, abyssal hills and extension of fracture zones.	Sparse	Very low/negligible abundance; small irregular nodules.	Sparse
Area 2 Siliceous	Diluted influence of Ganga-Brahmaputra rivers up to 8°S. High sedimentation rates.	Few seamounts; abundant abyssal hills.	Limited	Patchy distribution, small flattened nodules.	Glass shards, palagonite, phillipsite in sediments.
Area 3 Siliceous	High biological productivity and low sedimentation rates.	High relief area with number of seamounts (few cratered) and abyssal hills. Three major fracture zones at 73°E, 75°45'E and 79°E	Most abundant	Prime areas of nodule deposits. High abundance (>10 kg/m²) and high grade (>2.5%) Fe-Mn crusts.	Basalts (as outcrops and fragments), pumice clasts dominant, glass shards, volcanic spherules. A large pumice field demar cated. Occurrence of zeolite slabs.
Area 4 Calcareous			DATA NOT AVAILABLE		
Area 5 Pelagic-Brown clay	Low biological productivity.	Chains of seamounts and abyssal hills, number of small ridges extensions of all three major fracture zones.	Abundant	Extensions of prime areas. High abundances (5–10 kg/m²), low grade nodules (<2.5%)	Basalts, few pumice. Part of the pumice field falls in this area. Few locations of zeolite slabs.

Table 6: Correlation coefficient matrix of nodules from (a) siliceous sediment (n = 21), (b) siliceous-red clay transition sediment (n = 7) and (c) red clay sediment (n = 7). ΣREY is in ppm, rest all are in wt%. Values in bold have confidence level >99.9%.

	Fe %	**Mn %**	**Co %**	**Ni %**	**Cu %**	**Zr %**	**Mn/Fe**	**∑REY**
Fe %	1.00							
Mn %	-0.21	1.00						
Co %	**0.64**	-0.30	1.00					
Ni %	-0.36	0.39	**-0.81**	1.00				
Cu %	**-0.59**	0.22	**-0.80**	**0.86**	1.00			
Zr %	0.27	**-0.56**	**0.62**	**-0.76**	**-0.72**	1.00		
Mn/Fe	**-0.68**	**0.79**	**-0.54**	0.35	0.38	-0.42	1.00	
∑REY	**0.59**	-0.32	**0.94**	**-0.85**	**-0.91**	**0.76**	-0.47	1.00

(a)

	Fe %	**Mn %**	**Co %**	**Ni %**	**Cu %**	**Zr %**	**Mn/Fe**	**∑REY**
Fe %	1.00							
Mn %	0.21	1.00						
Co %	**0.79**	0.38	1.00					
Ni %	-0.71	-0.44	-0.52	1.00				
Cu %	**-0.94**	0.10	-0.63	0.63	1.00			
Zr %	-0.49	-0.72	-0.19	0.62	0.33	1.00		
Mn/Fe	-0.66	0.58	-0.40	0.19	**0.84**	-0.17	1.00	
∑REY	**0.81**	0.00	**0.90**	-0.40	-0.76	0.02	-0.71	1.00

(b)

	Fe %	**Mn %**	**Co %**	**Ni %**	**Cu %**	**Zr %**	**Mn/Fe**	**∑REY**
Fe %	1.00							
Mn %	-0.33	1.00						
Co %	**0.84**	-0.02	1.00					
Ni %	**-0.82**	0.49	-0.78	1.00				
Cu %	-0.70	0.68	-0.61	**0.85**	1.00			
Zr %	-0.38	-0.39	-0.23	0.19	-0.23	1.00		
Mn/Fe	**-0.87**	0.73	-0.64	**0.79**	**0.83**	-0.01	1.00	
∑REY	**0.84**	-0.25	**0.94**	-0.76	-0.76	0.04	-0.77	1.00

(c)